Published in final edited form as:
Hear Res. 2011 August ; 278(1-2): 52–68. doi:10.1016/j.heares.2011.01.016.

Complex distribution patterns of voltage-gated calcium channel α-subunits in the spiral ganglion

Wei Chun Chen[1], **Hui Zhong Xue**[1], **Yun (Lucy) Hsu**[2], **Qing Liu**[1], **Shail Patel**[3], and **Robin L. Davis**[1]

[1]Department of Cell Biology & Neuroscience, Rutgers University

[2]Department of Biochemistry & Microbiology, Rutgers University

[3]UMDNJ New Jersey Medical School

Abstract

As with other elements of the peripheral auditory system, spiral ganglion neurons display specializations that vary as a function of location along the tonotopic axis. Previous work has shown that voltage-gated K^+ channels and synaptic proteins show graded changes in their density that confers rapid responsiveness to neurons in the high frequency, basal region of the cochlea and slower, more maintained responsiveness to neurons in the low frequency, apical region of the cochlea. In order to understand how voltage-gated calcium channels (VGCCs) may contribute to these diverse phenotypes, we identified the VGCC α-subunits expressed in the ganglion, investigated aspects of Ca^{2+}-dependent neuronal firing patterns, and mapped the intracellular and intercellular distributions of seven VGCC α-subunits in the spiral ganglion *in vitro*.

Initial experiments with qRT-PCR showed that eight of the ten known VGCC α-subunits were expressed in the ganglion and electrophysiological analysis revealed firing patterns that were consistent with the presence of both LVA and HVA Ca^{2+} channels. Moreover, we were able to study seven of the α-subunits with immunocytochemistry, and we found that all were present in spiral ganglion neurons, and that three of them were neuron-specific ($Ca_V1.3$, $Ca_V2.2$, and $Ca_V3.3$). Further characterization of neuron-specific α-subunits showed that $Ca_V1.3$ and $Ca_V3.3$ were tonotopically-distributed, whereas $Ca_V2.2$ was uniformly distributed in apical and basal neurons. Multiple VGCC α-subunits were also immunolocalized to Schwann cells, having distinct intracellular localizations, and, significantly, appearing to distinguish putative compact0 ($Ca_V2.3$, $Ca_V3.1$) from loose ($Ca_V1.2$) myelin.

Electrophysiological evaluation of spiral ganglion neurons in the presence of TEA revealed Ca^{2+} plateau potentials with slopes that varied proportionately with the cochlear region from which neurons were isolated. Because afterhyperpolarizations were minimal or absent under these conditions, we hypothesize that differential density and/or kinetics of one or more of the VGCC α-subunits could account for observed tonotopic differences. These experiments have set the stage for defining the clear multiplicity of functional control in neurons and Schwann cells of the spiral ganglion.

Corresponding author: Dr. Robin L Davis, Department of Cell Biology & Neuroscience, 604 Allison Road, Nelson Laboratories, Rutgers University, Piscataway, NJ 08854, rldavis@rci.rutgers.edu Phone: 732-445-0440, FAX: 7332-445-5870.

Keywords

Spiral ganglion neurons; primary afferents; firing patterns; ion channels; calcium channels; VGCC; myelin; Schwann cells

Introduction

Neurons that comprise the spiral ganglion display a constellation of specialized features that vary systematically along the length of the cochlea. Although these primary sensory afferents were initially considered to be virtually identical, we and others have shown that, much like other elements in the auditory system, spiral ganglion neurons possess a high degree of electrophysiological and morphological sophistication (Davis and Liu, Submitted; Rusznak and Szucs, 2009; Ryugo, 1992), which is under precise regulatory control (Davis, 2003; Flores-Otero et al., 2007). This recently recognized level of complexity has provided novel insights into peripheral auditory coding and suggested new approaches to clinical remediation (Coleman et al., 2007; Pettingill et al., 2007).

Evidence for tonotopic specialization comes from both electrophysiological and immunocytochemical studies (Adamson et al., 2002b). Neurons that code high frequency auditory signals display rapid kinetic features, such as abbreviated action potential duration, reduced latency to spike, and rapid accommodation. Neurons that code low frequency auditory signals display distinctly slower kinetic features. They fire with prolonged action potential duration, increased latency to spike, and a mixture of rapid to slow accommodation. At the synaptic level, the presynaptic proteins, synaptophysin and synaptosomal-associated protein 25 (SNAP-25), and postsynaptic AMPA receptors, GluR2 and GluR3, are also distributed tonotopically (Flores-Otero et al., 2007). Importantly, both the firing features and synaptic compositions are controlled jointly by brain derived neurotrophic factor (BDNF) and neurotrophin-3 (NT-3), providing a mechanism for comprehensive regulation of electrophysiological phenotype as a function of location along the cochlea.

An interesting feature of the tonotopic gradients is that they display a superimposed regional variation. This has been documented electrophysiologically (Liu and Davis, 2007) using a "gangliotopic" culture preparation that preserves the cochlear architecture *in vitro* as well as by observation of an exquisitely arrayed gradient orthogonal to the tonotopic map *in vivo* (Flores-Otero and Davis, In The Press). One reason for the local variation appears to be production of overlaid, non-tonotopic gradations in other electrophysiological parameters. To date, we have found that two regulators of neuron excitably, resting membrane potential and voltage threshold level, both show non-monotonic distributions across the extent of the ganglion (Liu and Davis, 2007; Liu et al., 2010). Thus, consistent with behavioral and electrophysiological assessments *in vivo* (Müller and Smolders, 2005; Taberner and Liberman, 2005), spiral ganglion neurons independent of their peripheral and central targets *in vitro* also show the greatest sensitivity in the mid-cochlear range.

Although considerable inroads that have been made to understand better the complex distribution of electrophysiologically-relevant phenotypes within the spiral ganglion, the picture is not complete without an evaluation of voltage-gated calcium channels (VGCCs), a highly complex family of ion channels that serve diverse functional and regulatory roles (Dolphin, 2009; French and Zamponi, 2005). To date, ten VGCC α-subunits grouped into 3 families have been identified: Cav1 (high-voltage activated [HVA]; L-type); Cav2 (HVA; P/Q, N, and R-type), and Cav3 (low-voltage activated [LVA]; T-type; Catterall et al., 2005). The relatively small number of VGCC α-subunits, compared, for example, to K^+ channel α-

subunits, belies the complexity of this class of voltage-gated ion channels. The diversity of VGCCs is greatly amplified by mechanisms such as modifying regulatory subunits and splice variants (Gray et al., 2007; Jurkat-Rott and Lehmann-Horn, 2004).

Studies on VGCCs in the peripheral auditory system have mostly been done on hair cells. This work has shown that hair cells predominantly possess channels made up of L-type $Ca_V1.3$ subunits (Kollmar et al., 1997; Koschak et al., 2001; Platzer et al., 2000) with varying inactivation and activation rates along the tonotopic axis and throughout development (Johnson and Marcotti, 2008). However, less is known about VGCC composition in the primary afferents, especially with regard to cochlear distribution. Electrophysiological recordings show that the broad classes of L-, N-, and T-type currents are present in spiral ganglion neurons *in vitro* (Hisashi et al., 1995; Jimenez et al., 1997; Yamaguchi and Ohmori, 1990). The presence of the HVA Ca^{2+} channel α-subunits (Cav1.2, Cav1.3, Cav2.2 and Cav2.3) has been corroborated *in vivo* by RT-PCR and immunohistochemistry (Green et al., 1996; Lopez et al., 2003).

The study reported herein places these findings into the broader context of the ion channel gradients that we now know exist within the spiral ganglion. Quantitative (q) RT-PCR analysis showed that 8 α-subunits that were expressed in the ganglion, seven of which were examined further with available α-subunit specific antibodies. In addition, whole-cell patch clamp recordings were made to identify calcium-dependent aspects of spiral ganglion firing features. These approaches revealed a clear contribution of VGCCs to neuronal firing features as well as suggesting roles in putative myelinating, and non-myelinating Schwann cells. The complexity of the VGCC functional roles is evident simply from the fact that spiral ganglion neurons possessed all 7 α-subunits which were examined immunocytochemically, with differential intracellular and intercellular distributions that were unique to each. Notably, two of the three neuron-specific α-subunits ($Ca_V1.3$ and $Ca_V3.3$) were tonotopically-distributed; the third ($Ca_V2.2$) showed uniform luminance between neurons isolated from apical and basal regions. Moreover, deactivation and/or inactivation kinetics of one or more of the VGCC α-subunits could account for the plateau potentials observed in the presence of TEA that were clearly prolonged, with shallow slopes in apical neurons compared to middle and basal neurons. Multiple VGCC α-subunits were also localized to Schwann cells, having distinct intracellular localizations, and, significantly, appearing to distinguish compact ($Ca_V2.3$, $Ca_V3.1$) from loose myelin ($Ca_V1.2$). Although additional experiments are required to define the specific VGCC α-subunit footprint for each of our observations, the experiments presented herein have nevertheless set the stage for defining the contributions of VGCCs to neuronal and glial functions in the spiral ganglion.

Methods

Tissue culture

Procedures performed on CBA/CaJ mice were approved by The Rutgers University Institutional Review Board for the Use and Care of Animals (IRB-UCA), protocol 90-073. Spiral ganglia were removed from postnatal day (P) 6–7 mice following the procedures previously described (Adamson et al., 2002a) in which neuron somata are isolated from both their peripheral and central targets. The entire ganglion was utilized for qRT-PCR, while only the most apical and basal fifths of the ganglion were utilized for neuronal cultures. For cultures apical and basal sections were plated in tissue culture dishes coated with poly-ʟ-lysine. Neurons were maintained in growth medium containing Dulbecco's modified Eagle's medium (DMEM) supplemented with 10% fetal bovine serum, 4 mM L-glutamine, and 0.1% penicillin-streptomycin at 37°C in a humidified incubator with 5% CO_2 for 6–7 days *in vitro*.

qRT-PCR

Molecular techniques were performed following the procedures previously described (Chen and Davis, 2006). Briefly, total RNA was extracted from whole spiral ganglia (n = 3) using RNeasy mini kit (Qiagen), reverse-transcribed with SuperScript II RNase H-minus reverse transcriptase (Invitrogen), and amplified using SYBR Green-based PCR (Applied Biosystems). At each step, proper treatments (i.e. DNase I treatment during RNA isolation) and controls (i.e. Reverse-transcriptase-minus and non-template controls during PCR) were carried out. Specificity of all PCR products was confirmed by sequencing (DNA Sequencing and Synthesis Core Facility at University of Medicine and Dentistry at New Jersey-Robert Wood Johnson Medical School [UMDNJ-RWJMS], Piscataway, NJ).

Primer design—Primers for quantitative RT-PCR (Table 1) were designed using Primer Express Software 2.0 (Applied Biosystems) and their specificity was checked by comparing the nucleotide sequences of the PCR products to those of the NCBI genome database. All primers were synthesized at the DNA Sequencing and Synthesis Core Facility (UMDNJ-RWJMS).

Quantitative analysis—Sequence Detection System (SDS) 2.1 Software (Applied Biosystems) was used for analysis. To establish a guideline for evaluation, the baseline setting was adjusted between the 3rd and 15th cycle, at least two cycles before the earliest detection of PCR products. Threshold was adjusted within the middle-third (the exponential phase) of the amplification plot to optimize amplification efficiency (E). The same baseline setting and threshold were used for all three extracted groups. Standard curves were constructed to calculate the amplification efficiencies ($E = 10^{(-1/\text{slope})} - 1$) for all primers (Ginzinger, 2002). To compare amplification efficiencies between target and housekeeping (reference) gene, ΔC_t ($\Delta C_t = C_t$[Target] - C_t[Reference]) was plotted against the logarithm of cDNA dilution. A ΔC_t slope closer to zero means that the efficiencies between these genes are similar.

Immunocytochemistry

Indirect immunofluorescence—Immunostaining was performed following the procedures previously described (Flores-Otero et al., 2007). Preadsorption controls were evaluated for the following antibodies: anti-$Ca_v1.2$, $Ca_v2.3$, $Ca_v3.1$, and $Ca_v3.3$. The primary antibodies when pre-incubated with its respective antigen peptide (3 μg peptide and 1 μg antibody overnight) showed no immunolabeling in cultures. Furthermore, neuronal cultures treated with 2.5% NGS as a replacement for the primary antibodies showed no appreciable immunoreactivity with secondary antibodies alone.

Primary antibodies—Information for VGCC α-subunit antibodies used in this study is listed in Table 2. Anti-$Ca_V1.2$, $Ca_V2.1$, $Ca_V2.2$, $Ca_V2.3$, $Ca_V3.1$, $Ca_V3.3$ antibodies, obtained from Alomone Labs (Jerusalem, Israel), were characterized in an extensive study correlating immunocytochemical staining patterns to electrophysiological and molecular analyses using Western blot analysis (Nikitina et al., 2007). A subset of these antibodies ($Ca_V1.2$, $Ca_V2.1$, $Ca_V2.2$, $Ca_V2.3$) have also been examined in cochlear sections (Lopez et al., 2003). Anti-$Ca_v3.3$ antibody, directed against amino acids 1053–1067 in the intracellular loop between domain II and III, has also been characterized by Western blot analysis of transfected HEK 293 cells stably expressing $Ca_v3.3$ protein, which showed a single band at ~200 kD (Avila et al., 2009; Zhang et al., 2006) that was is absent in native HEK 293 cells. Anti-$Ca_V1.3$ antibody, obtained from NeuroMab (UC Davis/NIH), showed specific localization to ~250 kD with Western blot analysis. Although we measured relatively high $Ca_V3.2$ mRNA expression levels (Fig. 1c), specific antibodies that labeled ganglion cells were unavailable.

Anti-microtubule-associate protein 2 (MAP2; Millipore, Bilerica, MA) and anti-myelin basic protein (MBP; SMI-99, Sternberger Monoclonals, Lutherville, MD) were utilized to localize specific protein distributions within neurons and myelin, respectively. Both antibodies are well characterized in the literature (Blanchart et al., 2006; DeSilva et al., 2009) and are listed in the JCN antibody database.

Anti-class III β-tubulin antibody was utilized to distinguish spiral ganglion neurons from surrounding satellite cells in spiral ganglion cultures, either a polyclonal or monoclonal class III β-tubulin neuron-specific antibody was applied (Covance; Princeton, NJ). The class III β-tubulin neuronal antibody recognized a 50kDa molecular weight band in Western blot analysis of rat brain (1:5,000) and MDCK lysate (1:500; Covance; PRB-435P and MMS-407R datasheet, respectively). Previous studies from this laboratory have utilized anti β-tubulin labeling to demarcate neurons from background satellite cells at appropriate concentrations (Reid et al., 2004).

Secondary antibodies—Alexa-fluor 488-conjugated anti-mouse (Invitrogen 11017), Alexa-fluor 488-conjugated anti-rabbit (Invitrogen 11070), Alexa-fluor 594-conjugated anti-rabbit (Invitrogen 11072), Alexa-fluor 594-conjugated anti-mouse (Invitrogen 11020), and Alexa-fluor 350-conjugated anti-mouse (Invitrogen 11068) secondary antibodies were utilized in this study. Hoechst 33342 dye (Sigma-Aldrich) was utilized to localize cell nuclei.

Quantitative Analysis—Images were acquired with a Hamamatsu ORCA-ER camera on a Zeiss Axiovert 200M inverted microscope using IPLab 3.64 Scientific Imaging Processing. The same exposure time was used to acquire images within each experiment, and images processed in Adobe Photoshop and/or Corel Draw received the same digital enhancement. Using original IPLab images, antibody luminance was measured by subtracting the average of four background measurements from the average of three measurements taken from the brightest areas of neuronal cell body. Each evaluation of antibody labeling, generally consisting of over 100 measurements, was considered as a single experiment for data analysis and tests of significance.

Electrophysiology

Electrodes were coated with silicone-elastomer (Sylgard) and fire polished (Narishige MF-83). Resistances ranged from 4 to 6 MΩ in standard pipette and bath solutions. Pipette offset current was zeroed immediately before contacting the cell membrane. Current-clamp measurements were made with the I_{fast} circuitry of the Axon Instrument Axopatch 200A amplifier. The basic internal solution was as follows (in mM): 112 KCl, 2 $MgCl_2$, 0.1 $CaCl_2$, 11 EGTA, and 10 HEPES-KOH, pH 7.2. The bath solution (in mM) was 137 NaCl, 5 KCl, 1.7 $CaCl_2$, 1 $MgCl_2$, 17 glucose, 13 sucrose, and 10 HEPES-NaOH, pH 7.5; 330 mOsm. For selected experiments, rapid solution changes were achieved with a micro-perfusion system (Ogata and Tatebayashi, 1991). Toxins were prepared as stock solutions in distilled water and were dissolved into bath solution for application to neurons. The final concentration was 50 or 100 μM for cadmium chloride ($CdCl_2$) and 10 mM for tetraethylammonium chloride (TEA). Because we wished to determine whether spiral ganglion neurons possess Ca^{2+}-dependent plateau potentials, application of the broad spectrum K^+ channel blocker, such as TEA (Mathie et al., 1998) is appropriate for this purpose. Although TEA has been shown to affect the rate of Ca^{2+} channel inactivation when applied internally (Stotz et al., 2000), we expect that this would have little or no effect on recordings made herein since TEA was applied externally.

Recordings from the neuronal cell somata were made at room temperature (19–22°C), although differential temperature-dependent alterations have been noted in the current magnitude and kinetics (Cao and Oertel, 2005); the properties of voltage dependence, threshold, and adaptation were temperature insensitive (Cao and Oertel, 2005; Crumling and Saunders, 2005).

Data were digitized at 10 kHz with a CED Power 1401 interface in an IBM-compatible personal computer and filtered at 1 or 2 kHz; the programs for data acquisition and analysis were generously contributed by Dr. Mark R. Plummer, Rutgers University. Current-clamp recordings were considered acceptable when they met the following criteria: stable membrane potentials, low noise levels, discernible membrane time constant on step current injection, and overshooting action potentials (magnitudes of ≥70 mV). If any of these parameters changed during an experiment, indicating compromised cell health or metabolic failure, the remaining data were not included in the analysis.

Results

Identification of VGCC α-subunits in the spiral ganglion

In order to identify the VGCC α-subunits that contribute to shaping the primary afferent electrophysiological phenotype, we used acutely dissected tissue from isolated spiral ganglia for qRT-PCR analysis. Of the ten known Ca_V α-subunits, only two, $Ca_V1.1$ and $Ca_V1.4$, were expressed below detectable levels in the spiral ganglion. This finding is consistent with the specific expression of $Ca_V1.1$ in skeletal muscle and $Ca_V1.4$ in retina and dorsal root ganglia (Lipscombe et al., 2004). The remaining PCR products were observed at relatively high efficiencies and r^2 values (Fig. 1a) with amplification levels and thresholds that could be consistently distinguished from one another (Fig. 1b). Normalized C_t ratio with respect to β-actin revealed that of the eight α-subunits that could be detected in spiral ganglion, $Ca_V3.3$ and $Ca_V2.2$ had the lowest expression levels, while $Ca_V2.1$, $Ca_V2.3$ and $Ca_V3.1$ had the highest (Fig. 1c).

Analysis of these differences in expression level must take into account that mRNA isolated from the ganglion is contributed by satellite cells as well as by neurons. Schwann cells in particular are present in abundance and would therefore contribute strongly to the total mRNA that we analyzed. Because the satellite cells are more prevalent than the neurons, we speculated that mRNA expressed with the greatest abundance may be from satellite cells alone or in combination with neurons. Therefore, our expectation was that $Ca_V2.1$, $Ca_V2.3$ and $Ca_V3.1$ may be expressed widely throughout the ganglion, perhaps in multiple cell types, whereas $Ca_V3.3$ and $Ca_V2.2$ may be neuron-specific. These assumptions were explicitly tested in a later part of the study.

VGCCs shape the firing patterns of spiral ganglion neurons

To determine the basic electrophysiological contribution of VGCCs to the firing patterns of spiral ganglion neurons, we made whole-cell current clamp recordings from spiral ganglion neurons before and after the application of broad spectrum ion channel blockers. In the first series of experiments, application of TEA, which blocks a number of delayed rectifier K^+ channels (Mathie et al., 1998) was used to reveal Ca^{2+}-dependent plateau potentials. The rapid action potential upstroke which is characteristic of primary auditory afferents (Fig. 2a, black traces labeled with black circles) was, as expected, virtually unchanged after exposure to TEA (Fig. 2a, gray traces labeled with triangles, squares and diamonds for base, middle and apex, respectively). The repolarization phase, however, was dramatically altered, revealing the existence of a prolonged plateau phase which typifies the contribution of VGCCs (Mason and Leng, 1984; Storm, 1987; Sundgren-Andersson and Johansson, 1998).

Most neurons, regardless of whether they were taken from apical, middle or basal regions of the ganglion, displayed a prolonged plateau voltage after TEA exposure (Fig. 2b, arrows). It was evident, however, that cells from different locations showed different degrees of repolarization prolongation. From individual (Fig. 2c) and averaged (Fig. 2d) quantitative evaluations of action potential duration, the greatest effects of TEA were produced in apical and middle neurons as compared to basal ones (Fig. 2e). Interestingly, the relative relationships of action potential durations seen under control conditions (Adamson et al., 2002b) were retained even after the application of TEA (Fig. 2d). Along with this, we noted that the slopes of the prolonged plateaus were systematically different in apical, middle and basal spiral ganglion neurons (Fig 2b, inset). The individual recordings superimposed in Figure 2b, show the overall observations quantified in figure 2f, that the slope of the plateau is greater for basal neurons (−8.9 ± 1.7 mV/ms, n = 6) compared to middle (−7.0 ± −1.6 mV/ms, n = 6) and apical (−2.4 ± 0.7 mV/ms, n = 4; $p<0.05$) ones. Two apical neurons that did not display the plateau response, described below (Fig. 3), were eliminated from the analysis of slope (Fig 2f) in order to compare directly the measurements resulting from Ca^{2+} spikes.

A possible explanation for the tonotopic variation in action potential duration could be differences in K^+ channel composition that characterize spiral ganglion neurons from specific tonotopic locations (Adamson et al., 2002b). However, the recordings after TEA application generally showed an absence or dramatic reduction of a fast afterhyperpolarization (AHP), thus indicating that classic delayed rectifiers are sufficiently blocked under these conditions that they most likely no longer contribute to shaping the action potential profile. Therefore, one can also postulate that tonotopic variation in another feature, such as VGCC density, type, inactivation or deactivation kinetics could also account for or contribute to tonotopic variation in the voltage profile of the prolonged potential.

The plateau potential classically associated with VGCCs was observed in most of the recordings that were made. We did, however, note that this feature was lacking in a small proportion of neurons. Rather than displaying a dual phase repolarization after TEA exposure (Fig. 3, upper set of apex and base traces), these neurons showed a single phase typically associated with Na^+ channel inactivation in the presence of K^+ leak conductances (Fig. 3, middle set of apex traces). Even at suprathreshold voltages, when the plateau potential in most neurons becomes more pronounced (Fig 3, upper and lower series of traces, −49mV and −43 mV, respectively), the lack of the plateau potential in this small population of neurons was still observed (Fig. 3, middle traces, −43mV). To date we have only observed this lack of a plateau potential in apical neurons, which is consistent with the heterogeneity that is typically observed in spiral ganglion neurons innervating mid- to low frequency regions of the cochlea (Liu and Davis, 2007). Thus, we may expect to observe that VGCC density varies from neuron to neuron, especially in the apical region of the ganglion.

To explore more directly how VGCCs contribute to shaping spiral ganglion neuronal action potentials, we utilized $CdCl_2$, a broad spectrum Ca^{2+} channel blocker. This blocker had multiple effects, indicating the presence of both LVA and HVA VGCCs. Firstly, we noted that the latency of the action potential at threshold in control conditions (Fig. 4a, black traces labeled with triangles) was prolonged in neurons after exposure to $CdCl_2$, regardless of whether they were isolated from the apex, middle or base of the cochlea (Fig. 4a, gray traces labeled with diamonds). This indicates that LVA calcium channels have an effect on the firing patterns of these cells. Quantitative analysis for apical, middle and basal neurons for both individual (Fig. 4b) and averaged (Fig. 4c) data confirmed this observation, although the prolonged latencies that typify apical neurons in control conditions and the abbreviated latencies that typify basal neurons were altered to a somewhat lesser degree by $CdCl_2$

application than middle neurons (Fig. 4d) a difference that was, however, not statistically significant. VGCCs that activate at low voltage ranges, therefore, contribute to setting the latency to action potential firing, but may not be responsible for specifically shaping the graded changes. If this is the case, then one might expect to observe equal channel densities of the LVA Ca_V α-subunits that contribute to this feature.

Another change in the action potential profile of spiral ganglion neurons following the application of $CdCl_2$ was a systematic abbreviation of action potential duration. To visualize these changes, we aligned the action potentials (at threshold voltage) to the peak voltage for recordings from apex, middle and basal neurons before (Fig. 4e, black traces labeled with triangles) and after (Fig. 4e, gray traces labeled with diamonds) exposure to $CdCl_2$. These superimposed traces showed once again that the initial upstroke and amplitude of the action potentials were essentially unchanged, thus proving the stability of the recordings. The falling phase, however, was protracted in all cases. Examination of the control traces before and after $CdCl_2$ application revealed a subtle, but clear change in slope; this is exemplified for a middle neuron (Fig. 4e, middle black trace labeled with a triangle, arrows), but is also evident even in the most abbreviated action potential recorded in basal neurons (Fig. 4e, lower black trace labled with a triangle). Individual (Fig. 4f) and averaged (Fig. 4g) data indicate that action potential duration was altered systematically and significantly for apical, middle and basal neurons. The tonotopic difference was maintained after $CdCl_2$ exposure, such that the apical neurons were proportionally prolonged when compared to the basal neurons, supporting the role of K^+ channels in shaping the basic kinetic features of the initial action potential (Adamson et al., 2002b). In conjunction with this, apex and middle neurons showed a greater reduction in duration compared to basal ones (Fig. 4h), and although not statistically significant, this trend is consistent with our observations of slope differences after TEA exposure (Fig. 2f), thus leaving open the possibility that like voltage-gated K^+ channels, VGCCs may also contribute to the spiral ganglion's tonotopic electrophysiological features.

In summary, electrophysiological experiments using broad spectrum blockers have provided unequivocal evidence that LVA and HVA VGCCs contribute to shaping the action potential waveform in spiral ganglion neurons. They leave open the question of how the density and kinetics of VGCCs might be organized within the spiral ganglion. For example, should we find a VGCC α-subunit that is uniformly distributed within the ganglion we may draw a parallel with findings that kinetics, rather than channel density, is associated with the differing action potential durations and plateau slopes that were found between apical, middle and basal neurons. Conversely, tonotopic distribution of specific VGCC α-subunits at different densities could account for some of our observations. The immunocytochemical studies described below begin to address these questions.

Distribution patterns of neuron-specific VGCC α-subunits

The molecular and electrophysiological characterizations described above set the stage for evaluating the α-subunit types and distribution patterns across the tonotopic contour of the spiral ganglion, their local heterogeneity, and cell-type specific localization. Determining intercellular and intracellular distributions of thoroughly characterized anti-VGCC α-subunit antibodies will give us a starting point to evaluate the complexity and functional role of VGCCs in the primary auditory afferents. Our evaluations in this study are focused on spiral ganglion cultures, the same preparations in which the electrophysiology (described above) was carried out. Immunocytochemical evaluations showed that Cav1.3, Cav2.2, and Cav3.3 subunits were primarily neuronal, as predicted from the low mRNA expression levels found from acutely isolated spiral ganglion tissues.

$Ca_V1.3$ is enriched in basal spiral ganglion neurons—Of the four L-type channel α-subunits, only $Ca_V1.3$ was localized exclusively to the spiral ganglion neurons. As shown in figure 5 (panels a, b), anti-$Ca_V1.3$ α-subunit antibody labeled both apical and basal neurons; however, the luminance was enhanced in the high frequency basal cells. By comparison, anti-β-tubulin antibody labeling shown for the same region (Fig 5c, d), had relatively uniform luminance, indicating that staining penetration does not account for observed differences. Quantitative analysis of luminance for a single experiment plotted in a frequency histogram shows overlapping distributions for measurements taken from 289 apical and 186 basal neurons (Fig. 5e). Data normalized to the maximum observations and fitted with single Gaussians, highlight the differences between the mean values calculated for apical (370) basal neurons (455; Fig. 5f). Four separate experiments consistently showed that anti-$Ca_V1.3$ antibody luminance levels for basal neurons (552 ± 69) were significantly greater than those measured from apical neurons (396 ± 36, $p<0.05$; Fig. 5g).

As can be readily observed in figure 5 (panels a and b), anti-$Ca_V1.3$ antibody had a distinctive intracellular staining pattern. In both apical and basal neurons antibody labeling is clustered close to the region where one or both of the processes of these bipolar neurons originate (Fig. 5h, arrowhead). In some cases we have observed punctate labeling along the neurite processes (Fig. 5h, arrow). This staining pattern may reveal clues regarding specialized functions of the primary afferent neuronal somata.

$Ca_V2.2$ is uniformly distributed within the spiral ganglion—It is not surprising that the neuronal (N-type) $Ca_V2.2$ α-subunit is found predominantly in spiral ganglion neurons, but unlike the L-type $Ca_V1.3$ α-subunit, it is distributed uniformly throughout the spiral ganglion (Fig. 6a–b, d–e). From the perspective that most of the electrophysiologically-relevant proteins that we have investigated to date are differentially distributed within the ganglion, this is an intriguing finding. Quantitative analysis of luminance for a single experiment plotted in a frequency histogram shows overlapping distributions for measurements taken from 180 apical and 364 basal neurons (Fig. 6g). Normalized data show that the mean values calculated from single Gaussians for apical (208) basal neurons (228) essentially overlap (Fig. 6h). Three separate experiments consistently showed that anti-$Ca_V2.2$ antibody luminance levels were effectively the same for apical (205 ± 38) and basal neurons (216 ± 42; Fig. 6i).

Despite the uniformity throughout the ganglion, we noted that anti-$Ca_V2.2$ antibody labeling also had a distinctive intracellular distribution. As shown in figure 6 (panels a and b), the neuronal somata as well as the initial processes originating from either side of the cell soma were specifically labeled. Different from the clustered distribution noted for $Ca_V1.3$, the labeling of anti-$Ca_V2.2$ had a smooth appearance but unlike β-tubulin it was truncated, such that it only extended tens of microns (Fig. 6a, arrows) along the length of a neurite that could extend for hundreds of microns. Interestingly, this distribution corresponds to a labeling pattern that we observe with anti-MAP2 antibody. This microtubule associate protein, which demarcates dendritic and somatic regions of central neurons, distinctly labels spiral ganglion somata and the initial processes that project from it (Fig. 6c, f) and further highlights the specialized electrophysiological properties associated with the spiral ganglion neuronal somata.

$Ca_V3.3$ is enriched in basal spiral ganglion neurons—Spiral ganglion neuronal soma from distinct tonotopic regions also differentially label with anti-$Ca_V3.3$ α-subunit antibody (Fig. 7a–d). This LVA VGCC, which could contribute to enhancing the speed with which a neuron reaches threshold, was enriched in the high frequency basal neurons compared to apical neurons. Unlike the previous two, it did not have a distinctive subcellular distribution, although it did appear to be limited to the cell soma. Quantitative analysis of

luminance for a single experiment plotted in a frequency histogram shows overlapping distributions for measurements taken from 143 apical and 316 basal neurons (Fig. 7e). Normalized data, show that the mean values calculated from single Gaussians for apical (278) basal neurons (453; Fig. 7f) highlight the differences. Five separate experiments consistently showed that the enhanced anti-$Ca_V3.3$ antibody luminance levels for basal neurons (464 ± 73) differed significantly from those measured from apical neurons (298 ± 15, $p<0.05$; Fig. 7g).

VGCC subunits localized in satellite cells / myelin / neurons

As predicted from the high expression levels determined for $Ca_V1.2$, $Ca_V2.1$, $Ca_V2.3$, and $Ca_V3.1$, we found that these α-subunits were distributed in satellite cells as well as within spiral ganglion neurons. What is most notable about our findings, however, is the differential intracellular localization in satellite cells and distinctions in the distribution of VGCCs in myelin-like profiles surrounding the neuronal soma and processes.

$Ca_V1.2$ labels neurons, putative non-myelinating Schwann cells and loose myelin-like structures that encase neuronal somata—Unlike the neuron-specific labeling that we noted above, more extensive cell labeling was observed for the L-type anti-$Ca_V1.2$ α-subunit antibody. Not only did neighboring neurons appear to be differentially labeled, but the extensive processes of surrounding satellite cells made it a challenge to quantitatively assess neuronal luminance (Fig. 8a, d). Pre-adsorption controls preformed for this and other antibodies used in this study (Methods), showed little or no labeling when cultures were stained with anti-$Ca_V1.2$ pre-incubated with its antigen (Fig. 8b, e) or with secondary antibody alone (Fig. 8c, f).

Upon careful inspection, it was clear that small bipolar satellite cells having profiles similar to that reported for non-myelinating Schwann cells (Salzer and Bunge, 1980; Whitlon et al., 2010) were extensively labeled in both their soma and processes (Fig. 8g, arrowhead). These cells are aligned along neurite processes (Fig. 8g) and surround neuronal soma (Fig. 8j, arrowheads), often distorting the bipolar shape of ganglion cells (Fig. 8h, arrow). We also occasionally observed smooth or uniform labeling of structures that appeared to encase neuronal somata and associated putative Schwann cells (Fig. 8k–m). In addition, there was frequently a difference between the number of putative Schwann cells associated with a cell soma depending upon whether it was encapsulated or not. For example, only a single neuron and satellite cell are associated with the structure shown in Figures 8k–m (arrowheads), whereas the un-encapsulated soma in figure 8j is associated with several satellite cells. We speculate that this structure may represent the unique loose myelin that envelops the cell bodies of type I spiral ganglion neurons (Rosenbluth, 1962; Toesca, 1996). There was no evidence that anti-$Ca_V1.2$ α-subunit antibody labeled the myelin-like formations known to be present in these cultures along neurites (see below).

Cells with larger nuclei than the putative Schwann cells, which were unstained with anti-β-tubulin and thus classified as non-neuronal, were not labeled with the anti-$Ca_V1.2$ antibody (Fig. 8n, arrows). The spiral ganglion neurons themselves, however, were clearly labeled. This was most convincingly observed in cases in which the density of surrounding stained satellite cells was relatively low. The neurons depicted in figure 8 (panels o,p and q,r) are from the same experiment, yet one is brightly labeled (Fig. 8o) whereas the other is only lightly labeled (Fig. 8q), suggesting that subunit density is likely to be heterogeneous. The extensive satellite cell network surrounding most neurons precluded luminance measurements and estimates of tonotopic variation for the anti-$Ca_V1.2$ α-subunit antibody.

$Ca_V2.1$ is found primarily in the soma of non-myelinating Schwann cells and neurons—We found that the putative non-myelinating Schwann cells in our neuronal cultures were also labeled with anti-$Ca_V2.1$ α-subunit antibody, as were the spiral ganglion neurons. As shown in figure 9a, extensive labeling was seen on either side of the small nuclei (arrowheads) of the prevalent bipolar satellite cells situated next to the neuronal somata and along their neurites. Rarely, one could observe a process-like extension enveloping a neuron somata that appears to originate from a neighboring Schwann cell (Fig. 9b, arrow). Additionally, cytoplasmic labeling of anti-$Ca_V2.1$ was apparent in spiral ganglion neurons when surrounding satellite cells did not obstruct their visualization (Fig. 9c, d). In such cases, we noted a distinct pattern of intracellular labeling, such that pockets of non-labeled regions were interspersed between labeled regions (Fig. 9c). As with the anti-$Ca_V1.2$ α-subunit antibody, quantitative evaluations were prevented by the overlapping immunolabeled satellite cells.

$Ca_V2.3$ and Cav3.1 are localized to the neuronal somata, satellite cells, putative myelinating Schwann cells and compact myelin—Similar to the other VGCCs described above, the anti-$Ca_V2.3$ and anti-$Ca_V3.1$ antibodies labeled both neurons and satellite cells. An example of this is shown for the anti-$Ca_V2.3$ antibody in Figure 10. The high levels of non-neuronal and neuronal anti-$Ca_V2.3$ antibody labeling (Fig. 10a, b) that we typically observed were blocked in pre-adsorption and secondary antibody-alone controls (data not shown). In some cases, however, we were able to visualize individual neurons in isolation and determined that neighboring neurons displayed distinct heterogeneity. As shown in figure 10, some neurons were very brightly labeled (panels c, d), whereas most others were only lightly labeled or unlabeled (Fig. 10e, f). Quantitative assessments of neuronal luminance were not feasible due to typically high staining levels of the surrounding satellite cells, so we were unable to assess tonotopic distribution of $Ca_V2.3$.

An intriguing feature of the anti-$Ca_V2.3$ antibody was that it labeled structures resembling compact myelin; two different examples are shown in figure 10 (panels g–i and j–l). A subset of neurites were covered in what appeared to be a cylindrical sheath, such that β-tubulin labeling of the surrounded neurites appeared to be interrupted, and only regions on either side of the myelin-like structure were labeled with anti-β-tubulin antibody (Fig. 10g–i and j–l, arrows). In some cases we noted an enlargement that approximated the size and shape of the Schwann cell soma profiles shown in previous figures (Fig. 10i, arrowhead). In order to determine whether these stained profiles are consistent with the compact myelin that may form around spiral ganglion neuron processes, we labeled neuronal cultures with anti-myelin basic protein (MBP) antibody (SMI-99). Evaluations of anti-MBP immunolabeling revealed profiles that were remarkably similar to those seen with the anti-$Ca_V2.3$ antibody. Anti-MBP antibody labeled elongated segments (Fig. 10m, n, red), which appeared to be wrapped around β-tubulin-labeled neurites. The soma profile consistent with the size and shape of Schwann cells was also observed along the length of some fibers (Fig. 10m, arrowhead). Thus, the specificity of anti-MBP for myelin, along with the similarity of the structures stained, is consistent with the idea that anti-$Ca_V2.3$ antibody labels compact myelin. Interestingly, we didn't observe these $Ca_V2.3$-immunolabeled structures surrounding the neuronal soma, suggesting that compact myelin has a different VGCC composition than the putative loose myelin observed with $Ca_V1.2$ immunofluorescence.

The anti-$Ca_V3.1$ antibody staining pattern of the spiral ganglion cultures was somewhat similar to that of the anti-$Ca_V2.3$ antibody. A profusion of satellite cells (Fig. 11a, arrowhead) were labeled in addition to segments of compact myelin-like profiles that were bracketed by anti-β-tubulin immunolabeled neurites (Fig. 11a, arrows). Although not immediately evident in the overlay shown in Figure 11a, when the anti-$Ca_V3.1$ antibody is examined alone, it is clear that neurons are also immunolabeled (Fig. 11b, c); furthermore,

staining that was eliminated with preadsorption and secondary antibody controls. Quantitative analysis of luminance for a single experiment plotted in a frequency histogram shows overlapping distributions for measurements taken from 74 apical and 124 basal neurons (Fig. 11f). Data normalized to the maximum observations and fitted with single Gaussians, show that the mean values calculated for apical (145) basal neurons (133) essentially overlap. Three separate experiments showed anti-$Ca_V3.1$ antibody luminance levels did not differ systematically between apical and basal neurons (210 ± 37 and 328 ± 94, respectively; Fig. 11h).

Discussion

The mammalian action potential is an extraordinarily rich vehicle for information transmission in the nervous system (Bean, 2007). The sculpting of the waveform and firing characteristics by a complex combination of voltage- and time-dependent ionic currents allows tailoring of the action potential to specific purposes. A need for this sophistication is clearly evident in the auditory system, where speed of response and maintenance of timing relationships is critical for sound perception and localization (Joris and Yin, 2007). In previous work, we have shown that the voltage-gated K^+ channel and synaptic protein composition in spiral ganglion neurons differs according to whether they code high or low frequency sounds (Flores-Otero et al., 2007). In the present study, we have expanded this analysis to voltage-gated calcium channels, using molecular, electrophysiological, and immunocytochemical approaches to characterize neurons from different cochlear regions maintained *in vitro*. Our findings using TEA and $CdCl_2$ support a role for VGCCs in shaping electrophysiological response properties, and our immunocytochemical analysis has begun to define which channels may be the most important in contributing to spiral ganglion firing features.

The advantage of examining the distribution of VGCC α-subunits *in vitro* is four-fold. Firstly, it allows us to correlate our electrophysiological assessments with immunocytochemical evaluations. Secondly, having a better understanding of the complexity and distribution of VGCCs will assist us in designing more targeted electrophysiological experiments. Thirdly, the fact that a neuron or Schwann cell can be visualized in its entirety allows a straightforward assessment of intracellular ion channel distribution. And, fourthly, cultured neurons permit direct experimental alterations to evaluate regulatory controls of VGCC expression. Despite these advantages, however, it is important to compare our findings to evaluations made *in vivo* from postnatal or adult animals. Interestingly, we found that the results from spiral ganglion neurons *in vitro*, reported herein are, in general, comparable to those shown in adult animals *in vivo*, albeit with some notable differences. One such difference is the detection of $Ca_V2.1$. The α1a, or $Ca_V2.1$, α-subunit was reported to be undetectable in adult chinchilla spiral ganglion neurons (Lopez et al., 2003); this is in contrast to our observations with qRT-PCR and immunocytochemistry. Although a preponderance of putative non-myelinating Schwann cell immunoreactivity prevented quantitative assessments, we were nonetheless able to detect its unique intracellular distribution in cultured spiral ganglion neurons (Fig. 9). The other VGCCs evaluated in adult chinchilla spiral ganglion showed similarities to our findings. α1B, α1C, α1D and α1E, ($Ca_V2.2$, $Ca_V1.2$, $Ca_V1.3$, and $Ca_V2.3$, respectively) were all present in spiral ganglion neurons with various levels of heterogeneity, similar to what we observed *in vitro*. VGCC localization to Schwann cells and myelin has also been observed *in vitro*. The extensive immunolabeling of non-myelinating Schwann cells by anti-$Ca_V1.2$ has been observed in another sensory system *in vivo* (Westenbroek et al., 2004). Furthermore, our observations that $Ca_V1.2$, $Ca_V2.1$, $Ca_V2.3$ and $Ca_V3.1$ α-subunits are present in myelinating and non-myelinating Schwann cells is consistent with numerous

electrophysiological studies describing the localization of multiple VGCCs including L-type and T-type channels (Baker, 2002).

Intracellular VGCC α-subunit distributions

It is widely recognized that intracellular calcium signaling is extraordinarily complex and has cell type-dependent functional significance (Dolphin, 2009; Lipscombe et al., 2004). The impact of elevations of internal [Ca^{2+}] in neurons can range from transcriptional regulation to synaptic plasticity and electrical transmission (French and Zamponi, 2005). We have learned from examining the cellular localization of VGCC α-subunits in the spiral ganglion that the same principles apply to this seemingly simple peripheral cluster of neurons and satellite cells. The distinct subcellular distributions that we have characterized point to a multiplicity of functions subserved by the seven α-subunits that we were able to examine immunocytochemically. The most obvious differential distribution pattern is the localization of specific subunits to neurons and/or Schwann cells. All of the subunits that we examined, $Ca_V1.2$, $Ca_V1.3$, $Ca_V2.1$, $Ca_V2.2$, $Ca_V2.3$, $Ca_V3.1$, and $Ca_V3.3$ were localized to specific intracellular domains within the spiral ganglion neurons. While $Ca_V1.2$, $Ca_V2.1$, $Ca_V2.3$, $Ca_V3.1$, and $Ca_V3.3$ were diffusely localized to the neuronal soma (Fig. 12, cross hatches) and occasionally along neurites, antibodies against $Ca_V1.3$ and $Ca_V2.2$ had distinctly different staining patterns. $Ca_V1.3$, depicted by orange circles (Fig. 12), was enriched in regions generally associated with the initial processes that emerge from the cell soma and to punctate regions along the neurites. This pattern is reminiscent of the patchy distribution of Na^+ channels and CASPR in the cell body and nodes of spiral ganglion neurons *in vivo* (Hossain et al., 2005), and thus may be associated with shaping the action potential as it travels through the soma membrane and along the axon.

By contrast, $Ca_V2.2$, depicted by the green outline (Fig. 12), encompassed the entire cell soma as well as the tapered initial processes emanating from it. Because $Ca_V2.2$ (N-type) calcium channels are intimately associated with BK channels to carry out their function in shaping action potentials, we found it relevant that anti-BK and anti-BKβ4 antibodies displayed similar staining patterns (unpublished observations). This may indicate that spiral ganglion neurons are similar to hippocampal neurons where BK and N-type Ca^{2+} channels are functionally coupled (Loane et al., 2007). One might speculate that these interactions are also mediated by MAP2 based upon its similar cellular location in spiral ganglion neurons. We expect, nevertheless, that these associations are much more complex, especially considering that other types of VGCCs have been reported to be functionally coupled with BK (Sun et al., 2003), in addition to other classes of Ca^{2+}-dependent K^+ channels (Stocker, 2004).

The fact that Schwann cells possess multiple types of VGCCs is not surprising; the differential distribution of VGCCs between the putative compact myelin and loose myelin-like structures, however, is novel. The $Ca_V2.3$ and $Ca_V3.1$ α-subunits, depicted as gray horizontal bars, were detected in compact myelin-like ensheathments that were observed along the spiral ganglion neurites (Fig 12). The surrounding thin orange line surrounding the gray bars represents the close correspondence in structure that was observed with myelin basic protein immunoreactivity (Fig 12). $Ca_V1.2$ was distinctive in that beyond the non-myelinating Schwann cell labeling (light blue lines; Fig 12), it was also localized to sheath-like structures that appeared to encase the neuronal somata (light blue circular structure; Fig 12), yet no detectible anti-$Ca_V1.2$-labeled ensheathments were observed along the processes. This is notable because this result suggests an additional molecular distinction between the two types of myelin found in auditory and vestibular ganglion cells (Toesca, 1996).

Intercellular VGCC α-subunit distributions

The sophisticated organization of the spiral ganglion serves as a template for determining the frequency specificity of parameters that are differentially localized across the tonotopic axis. Voltage-gated K^+ channels and synaptic proteins have distinct distributions along the cochlear contour (Adamson et al., 2002b; Flores-Otero and Davis, In The Press; Liu and Davis, 2007) and are subject to precise regulation by neurotrophins (Adamson et al., 2002a; Flores-Otero et al., 2007). In order to understand the contribution of VGCCs to coding in the spiral ganglion, a similar analysis has been made herein.

The pervasive distribution of VGCCs, across multiple cell classes limited this type of analysis to the three α-subunits that were neuron-specific in the spiral ganglion: $Ca_V1.3$, $Ca_V2.2$, and $Ca_V3.3$. The enigmatic $Ca_V1.3$ was originally classified as an HVA L-type channel, but has since been shown to display distinctly non-HVA characteristics such as low-voltage activation with rapid kinetics (Lipscombe et al., 2004), characteristics which can be altered in the multiple splice variants that have been identified (Singh et al., 2008). Interestingly, the $Ca_V1.3$ splice variants are tonotopically localized in gerbil inner hair cells, thus altering inactivation such that it is faster in the high frequency region purportedly to support repeated synaptic vesicle release (Johnson and Marcotti, 2008). Taking these findings into account, one wonders whether $Ca_V1.3$ splice variants underlie or contribute to the graded slopes measured from the prolonged plateau potentials revealed with application of TEA. The distinct lack of a fast AHP indicates that calcium channel deactivation or inactivation kinetics could play a role, but since the neurons possess a wide array of VGCCs, and because we observe tonotopic immunolabeling patterns associated with $Ca_V1.3$ which is not necessarily predicted by alterations in splice variants alone, voltage clamp studies are currently underway in our laboratory to directly assess calcium channel current density and inactivation.

$Ca_V3.3$ LVA VGCCs are also organized tonotopically, such that their greatest density is in the high frequency, basal neurons. This pattern of $Ca_V3.3$ α-subunit immunolocalization mimics our previous observations of GluR2 and GluR3 AMPA receptor enrichment in the basal spiral ganglion neurons (Flores-Otero et al., 2007). Both tonotopic specializations could be utilized for similar purposes, to allow basal neurons, with their abundant voltage-gated ion channels, to overcome the resultant low input resistance in order to reach threshold.

The remaining neuron-specific α-subunit we characterized, $Ca_V2.2$, is truly an HVA VGCC, with multiple functions. Based upon its intercellular and intracellular staining patterns and its known role in regulating synaptic transmission and shaping the action potential waveform, we hypothesize that this α-subunit may play dual roles in the spiral ganglion. Perhaps the most predominant and consistent function of the N-type Ca^{2+} channel is in neurotransmitter release. Therefore, we expect that it plays the same role of regulating Ca^{2+} entry pre-synaptically in order to mediate vesicle fusion in spiral ganglion neurons. Furthermore, the $Ca_V2.2$ immunolocalization profile showed a unique pattern of intracellular labeling that essentially highlighted the soma and initial processes emanating from it. We noted similarities between this staining pattern and those observed with anti-BKβ4 and anti-BK antibody labeling (unpublished observations). Interestingly, these same patterns correspond to the soma and initial process immunolabeling of MAP2, a traditional dendritic and neuronal somata marker (Arimura and Kaibuchi, 2007; Goedert et al., 1991). Such co-localizations indicate that the functional interactions which have been characterized between this N-type Ca^{2+} channel and the BK channel (Loane et al., 2007) may occur within a unique intracellular area of the spiral ganglion neuron, defined by MAP2.

Each of the N-type channel functions described above predicts opposite $Ca_V2.2$ distribution patterns. The association with BK channels, which are highly enriched in the basal neurons, predicts a high frequency regional localization. Conversely, the association with presynaptic proteins, which are highly enriched in apical neurons, predicts a low frequency regional localization. Interestingly, the $Ca_V2.2$ a-subunit is unique amongst the ion channels that we have heretofore evaluated, in that it displays a relatively uniform intercellular distribution that is consistent with dual functions requiring opposite tonotopic distributions.

A hallmark of VGCC α-subunit distribution, whether uniform or graded along the tonotopic contour, is regional heterogeneity. Most heterogeneous of all is $Ca_V2.3$, having only few neurons that were highly enriched for the α-subunit. Nevertheless, consistent with observations from adult *in vivo* immunostaining (Lopez et al., 2003), we noted that $Ca_V1.2$, $Ca_V1.3$, $Ca_V2.2$, $Ca_V3.1$, and $Ca_V3.3$, all showed various degrees of local heterogeneous immunolabeling. This aspect should not be overlooked, since it reflects the variation in electrophysiological properties revealed from both *in vitro* (Liu and Davis, 2007; Mo and Davis, 1997a; Mo and Davis, 1997b) and *in vivo* (Kiang et al., 1965; Liberman, 1982; Taberner and Liberman, 2005) studies. Moreover, it is consistent with the idea that the VGCCs contribute to the distinct differences that have been characterized for spiral ganglion neurons, ~95% of which form a divergent afferent pathway that is classically associated with parallel processing in sensory systems. This augurs well for the idea that regional differences in spiral ganglion neuron phenotype are important for neuronal coding functions.

In summary, analysis of VGCC mRNA expression, Ca^{2+}-dependent contributions to action potential waveform and VGCC α-subunit distributions in the spiral ganglion has revealed an emerging picture of phenotypic complexity and sophistication. Beyond shaping the electrophysiological response properties of these neurons and their surrounding Schwann cells, we expect that studying this elaborate class of voltage-gated ion channel types will lead to new insights into ganglion function due to the extensive long- and short-term regulatory effects triggered by changes in the concentration of intracellular Ca^{2+}.

Acknowledgments

We thank Edmund Lee for his help in manuscript preparation and data analysis and Dr. Mark R. Plummer for a critical reading of this manuscript. Work was supported by NIH NIDCD R01 DC-0856.

Reference List

Adamson CL, Reid MA, Davis RL. Opposite actions of brain-derived neurotrophic factor and neurotrophin- 3 on firing features and ion channel composition of murine spiral ganglion neurons. J Neurosci. 2002a; 22:1385–1396. [PubMed: 11850465]

Adamson CL, Reid MA, Mo ZL, Bowne-English J, Davis RL. Firing features and potassium channel content of murine spiral ganglion neurons vary with cochlear location. J Comp Neurol. 2002b; 447:331–350. [PubMed: 11992520]

Arimura N, Kaibuchi K. Neuronal polarity: from extracellular signals to intracellular mechanisms. Nat Rev Neurosci. 2007; 8:194–205. [PubMed: 17311006]

Avila T, Hernandez-Hernandez O, Almanza A, de Leon MB, Urban M, Soto E, Cisneros B, Felix R. Regulation of Ca v 3.1 channels by glucocorticoids. Cell Mol Neurobiol. 2009; 29:1265–1273. [PubMed: 19533336]

Baker MD. Electrophysiology of mammalian Schwann cells. Prog Biophys Mol Biol. 2002; 78:83–103. [PubMed: 12429109]

Bean BP. The action potential in mammalian central neurons. Nat Rev Neurosci. 2007; 8:451–465. [PubMed: 17514198]

Blanchart A, De Carlos JA, Lopez-Mascaraque L. Time frame of mitral cell development in the mice olfactory bulb. J Comp Neurol. 2006; 496:529–543. [PubMed: 16572431]

Cao XJ, Oertel D. Temperature affects voltage-sensitive conductances differentially in octopus cells of the mammalian cochlear nucleus. J Neurophysiol. 2005; 94:821–832. [PubMed: 15800074]

Catterall WA, Perez-Reyes E, Snutch TP, Striessnig J. International Union of Pharmacology. XLVIII. Nomenclature and structure-function relationships of voltage-gated calcium channels. Pharmacol Rev. 2005; 57:411–425. [PubMed: 16382099]

Chen WC, Davis RL. Voltage-gated and two-pore-domain potassium channels in murine spiral ganglion neurons. Hear Res. 2006; 222:89–99. [PubMed: 17079103]

Coleman B, de Silva MG, Shepherd RK. Concise review: the potential of stem cells for auditory neuron generation and replacement. Stem Cells. 2007; 25:2685–2694. [PubMed: 17656641]

Crumling MA, Saunders JC. Temperature insensitivity of short-term adaptation in single-units of the chick cochlear nerve. Synapse. 2005; 58:243–248. [PubMed: 16206182]

Davis RL. Gradients of neurotrophins, ion channels and tuning in the cochlea. Neuroscientist. 2003; 9:311–316. [PubMed: 14580116]

Davis RL, Liu Q. Complex primary afferents: What the distribution of electrophysiologically-relevant phenotypes within the spiral ganglion tells us about peripheral neural coding. Hear Res. Submitted.

DeSilva TM, Kabakov AY, Goldhoff PE, Volpe JJ, Rosenberg PA. Regulation of glutamate transport in developing rat oligodendrocytes. J Neurosci. 2009; 29:7898–7908. [PubMed: 19535601]

Dolphin AC. Calcium channel diversity: multiple roles of calcium channel subunits. Curr Opin Neurobiol. 2009; 19:237–244. [PubMed: 19559597]

Flores-Otero J, Davis RL. Synaptic proteins are tonotopically graded in postnatal and adult type I and type II spiral ganglion neurons. J Comp Neurol. In The Press.

Flores-Otero J, Xue HZ, Davis RL. Reciprocal regulation of presynaptic and postsynaptic proteins in bipolar spiral ganglion neurons by neurotrophins. J Neurosci. 2007; 27:14023–14034. [PubMed: 18094241]

French RJ, Zamponi GW. Voltage-gated sodium and calcium channels in nerve, muscle, and heart. IEEE Trans Nanobioscience. 2005; 4:58–69. [PubMed: 15816172]

Ginzinger DG. Gene quantification using real-time quantitative PCR: an emerging technology hits the mainstream. Exp Hematol. 2002; 30:503–512. [PubMed: 12063017]

Goedert M, Crowther RA, Garner CC. Molecular characterization of microtubule-associated proteins tau and MAP2. Trends Neurosci. 1991; 14:193–199. [PubMed: 1713721]

Gray AC, Raingo J, Lipscombe D. Neuronal calcium channels: splicing for optimal performance. Cell Calcium. 2007; 42:409–417. [PubMed: 17512586]

Green GE, Khan KM, Beisel DW, Drescher MJ, Hatfield JS, Drescher DG. Calcium channel subunits in the mouse cochlea. J Neurochem. 1996; 67:37–45. [PubMed: 8667015]

Hisashi K, Nakagawa T, Yasuda T, Kimitsuki T, Komune S, Komiyama S. Voltage-dependent Ca2+ channels in the spiral ganglion cells of guinea pig cochlea. Hear Res. 1995; 91:196–201. [PubMed: 8647721]

Hossain WA, Antic SD, Yang Y, Rasband MN, Morest DK. Where is the spike generator of the cochlear nerve? Voltage-gated sodium channels in the mouse cochlea. J Neurosci. 2005; 25:6857–6868. [PubMed: 16033895]

Jimenez C, Gireldez F, Represa J, Garcia-Diaz JF. Calcium currents in dissociated cochlear neurons from the chick embryo and their modification by neurotrophin-3. Neuroscience. 1997; 77:673–682. [PubMed: 9070744]

Johnson SL, Marcotti W. Biophysical properties of CaV1.3 calcium channels in gerbil inner hair cells. J Physiol. 2008; 586:1029–1042. [PubMed: 18174213]

Joris P, Yin TC. A matter of time: internal delays in binaural processing. Trends Neurosci. 2007; 30:70–78. [PubMed: 17188761]

Jurkat-Rott K, Lehmann-Horn F. The impact of splice isoforms on voltage-gated calcium channel alpha1 subunits. J Physiol. 2004; 554:609–619. [PubMed: 14645450]

Kiang, NY.; Watanabe, T.; Thomas, EC.; Clark, LF. Discharge Patterns of single fibers in the cat's auditory nerve. Cambridege, Massachusetts: The M.I.T. Press; 1965. p. 35

Kollmar R, Montgomery LG, Fak J, Henry LJ, Hudspeth AJ. Predominance of the alpha1D subunit in L-type voltage-gated Ca2+ channels of hair cells in the chicken's cochlea. Proc Natl Acad Sci U S A. 1997; 94:14883–14888. [PubMed: 9405708]

Koschak A, Reimer D, Huber I, Grabner M, Glossmann H, Engel J, Striessnig J. alpha 1D (Cav1.3) subunits can form l-type Ca2+ channels activating at negative voltages. J Biol Chem. 2001; 276:22100–22106. [PubMed: 11285265]

Liberman MC. Single-neuron labeling in the cat auditory nerve. Science. 1982; 216:1239–1241. [PubMed: 7079757]

Lipscombe D, Helton TD, Xu W. L-type calcium channels: the low down. J Neurophysiol. 2004; 92:2633–2641. [PubMed: 15486420]

Liu Q, Davis RL. Regional specification of threshold sensitivity and response time in CBA/CaJ mouse spiral ganglion neurons. J Neurophysiol. 2007; 98:2215–2222. [PubMed: 17715200]

Liu Q, Lee E, Davis RL. Ionic mechanisms that regulate murine spiral ganglion neuron firing excitability. Abstracts of the Association of Research for Otolaryngology. 2010; (33):741.

Loane DJ, Lima PA, Marrion NV. Co-assembly of N-type Ca2+ and BK channels underlies functional coupling in rat brain. J Cell Sci. 2007; 120:985–995. [PubMed: 17311846]

Lopez I, Ishiyama G, Acuna D, Ishiyama A, Baloh RW. Immunolocalization of voltage-gated calcium channel alpha1 subunits in the chinchilla cochlea. Cell Tissue Res. 2003; 313:177–186. [PubMed: 12845523]

Mason WT, Leng G. Complex action potential waveform recorded from supraoptic and paraventricular neurones of the rat: evidence for sodium and calcium spike components at different membrane sites. Exp Brain Res. 1984; 56:135–143. [PubMed: 6468562]

Mathie A, Wooltorton JR, Watkins CS. Voltage-activated potassium channels in mammalian neurons and their block by novel pharmacological agents. Gen Pharmacol. 1998; 30:13–24. [PubMed: 9457476]

Mo ZL, Davis RL. Endogenous firing patterns of murine spiral ganglion neurons. J Neurophysiol. 1997a; 77:1294–1305. [PubMed: 9084597]

Mo Z-L, Davis RL. Heterogeneous voltage dependence of inward rectifier currents in spiral ganglion neurons. J Neurophysiol. 1997b; 78:3019–3027. [PubMed: 9405521]

Müller M, Smolders JW. Shift in the cochlear place-frequency map after noise damage in the mouse. Neuroreport. 2005; 16:1183–1187. [PubMed: 16012345]

Nikitina E, Zhang ZD, Kawashima A, Jahromi BS, Bouryi VA, Takahashi M, Xie A, Macdonald RL. Voltage-dependent calcium channels of dog basilar artery. J Physiol. 2007; 580:523–541. [PubMed: 17185332]

Ogata N, Tatebayashi H. A simple and multi-purpose "concentration-clamp" method for rapid superfusion. J Neurosci Methods. 1991; 39:175–183. [PubMed: 1724682]

Pettingill LN, Richardson RT, Wise AK, O'Leary SJ, Shepherd RK. Neurotrophic factors and neural prostheses: potential clinical applications based upon findings in the auditory system. IEEE Trans Biomed Eng. 2007; 54:1138–1148. [PubMed: 17551571]

Platzer J, Engel J, Schrott-Fischer A, Stephan K, Bova S, Chen H, Zheng H, Striessnig J. Congenital deafness and sinoatrial node dysfunction in mice lacking class D L-type Ca2+ channels. Cell. 2000; 102:89–97. [PubMed: 10929716]

Reid MA, Flores-Otero J, Davis RL. Firing patterns of type II spiral ganglion neurons in vitro. J Neurosci. 2004; 24:733–742. [PubMed: 14736859]

Rosenbluth J. The fine structure of acoustic ganglia in the rat. J Cell Biol. 1962; 12:329–359. [PubMed: 14493992]

Rusznak Z, Szucs G. Spiral ganglion neurones: an overview of morphology, firing behaviour, ionic channels and function. Pflugers Arch. 2009; 457:1303–1325. [PubMed: 18777041]

Ryugo, DK. The auditory nerve: Peripheral innervation cell body morphology, and central projections. In: Webster, DB.; Popper, AN.; Fay, RR., editors. The Mammalian Auditory Pathway: Neuroanatomy. New York: Springer-Verlag; 1992. p. 23-65.

Salzer JL, Bunge RP. Studies of Schwann cell proliferation. I. An analysis in tissue culture of proliferation during development, Wallerian degeneration, and direct injury. J Cell Biol. 1980; 84:739–752. [PubMed: 6244318]

Singh A, Gebhart M, Fritsch R, Sinnegger-Brauns MJ, Poggiani C, Hoda JC, Engel J, Romanin C, Striessnig J, Koschak A. Modulation of voltage- and Ca2+-dependent gating of CaV1.3 L-type calcium channels by alternative splicing of a C-terminal regulatory domain. J Biol Chem. 2008; 283:20733–20744. [PubMed: 18482979]

Stocker M. Ca(2+)-activated K+ channels: molecular determinants and function of the SK family. Nat Rev Neurosci. 2004; 5:758–770. [PubMed: 15378036]

Storm JF. Action potential repolarization and a fast after-hyperpolarization in rat hippocampal pyramidal cells. J Physiol (Lond). 1987; 385:733–759. [PubMed: 2443676]

Stotz SC, Hamid J, Spaetgens RL, Jarvis SE, Zamponi GW. Fast inactivation of voltage-dependent calcium channels. A hinged-lid mechanism? J Biol Chem. 2000; 275:24575–24582. [PubMed: 10823819]

Sun X, Gu XQ, Haddad GG. Calcium influx via L- and N-type calcium channels activates a transient large-conductance Ca2+-activated K+ current in mouse neocortical pyramidal neurons. J Neurosci. 2003; 23:3639–3648. [PubMed: 12736335]

Sundgren-Andersson AK, Johansson S. Calcium spikes and calcium currents in neurons from the medial preoptic nucleus of rat. Brain Res. 1998; 783:194–209. [PubMed: 9507126]

Taberner AM, Liberman MC. Response properties of single auditory nerve fibers in the mouse. J Neurophysiol. 2005; 93:557–569. [PubMed: 15456804]

Toesca A. Central and peripheral myelin in the rat cochlear and vestibular nerves. Neurosci Lett. 1996; 221:21–24. [PubMed: 9014171]

Westenbroek RE, Anderson NL, Byers MR. Altered localization of Cav1.2 (L-type) calcium channels in nerve fibers, Schwann cells, odontoblasts, and fibroblasts of tooth pulp after tooth injury. J Neurosci Res. 2004; 75:371–383. [PubMed: 14743450]

Whitlon DS, Tieu D, Grover M. Purification and transfection of cochlear Schwann cells. Neuroscience. 2010; 171:23–30. [PubMed: 20837108]

Yamaguchi K, Ohmori H. Voltage-gated and chemically gated ionic channels in the cultured cochlear ganglion neurone of the chick. J Physiol (Lond). 1990; 420:185–206. [PubMed: 1691290]

Zhang D, Chen J, Saraf A, Cassar S, Han P, Rogers JC, Brioni JD, Sullivan JP, Gopalakrishnan M. Association of Catsper1 or −2 with Ca(v)3.3 leads to suppression of T-type calcium channel activity. J Biol Chem. 2006; 281:22332–22341. [PubMed: 16740636]

a

Spiral ganglion gene expression profile

Name	C_t[a]	PCR Efficiency[b]	r^2[c]	Δc_t slope[d]
$Ca_v1.2$	33.1 ± 1.0	95 ± 1	0.998	0.01
$Ca_v1.3$	33.4 ± 1.3	92 ± 2	0.998	0.09
$Ca_v2.1$	29.9 ± 0.8	99 ± 1	0.997	0.03
$Ca_v2.2$	34.6 ± 1.3	99 ± 2	0.998	0.08
$Ca_v2.3$	30.1 ± 1.0	97 ± 4	0.998	0.08
$Ca_v3.1$	29.6 ± 0.9	100 ± 4	0.999	0.14
$Ca_v3.2$	31.5 ± 1.0	94 ± 1	0.996	0.06
$Ca_v3.3$	37.2 ± 0.8	96 ± 2	0.996	0.05
β-actin	21.9 ± 0.6	97 ± 2	0.996	---

$Ca_v1.1$ and $Ca_v1.4$ are below the detectable range

C_t: cycle threshold.

[b] PCR efficiency (E) calculated from $E = (10^{(-1/\text{slope})}) - 1 \times 100\%$.

[c] r^2: coefficient of determination calculated from standard curves.

[d] ΔC_t slope: absolute value between target and β-actin genes.

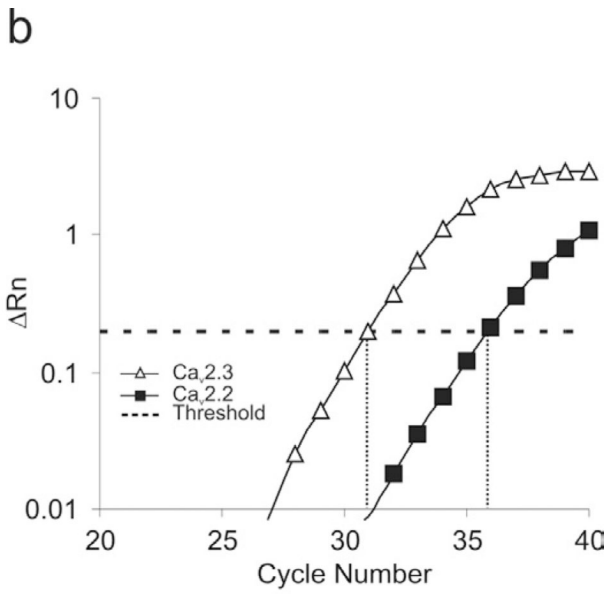

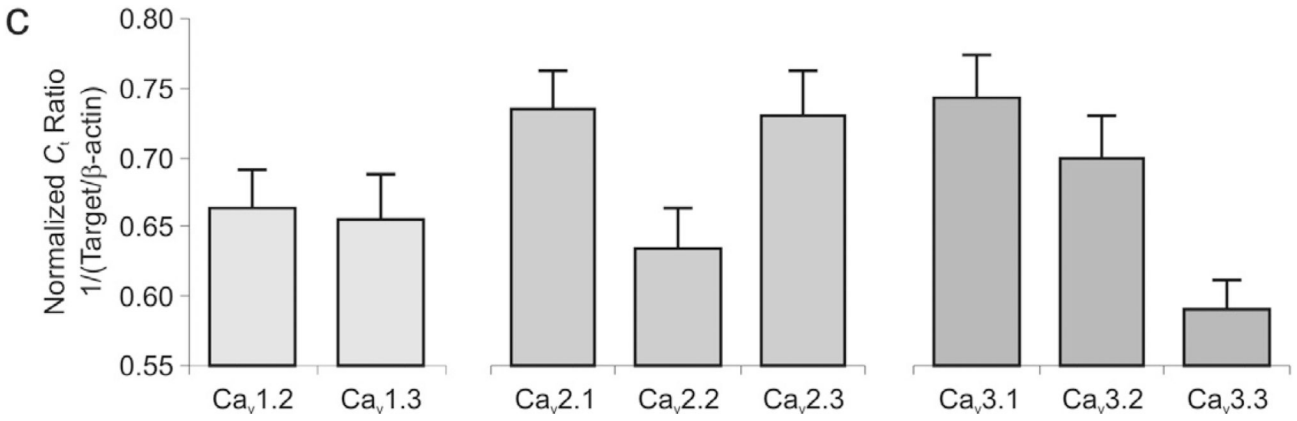

Figure 1.

VGCC α-subunit transcript expression levels in the spiral ganglion. (a) Survey of relative mRNA levels of Ca_v α-subunits. (b) An example of real-time qRT-PCR amplification of Ca_v mRNA transcripts shows a higher expression of $Ca_v2.3$ than $Ca_v2.2$. (c) Normalized C_t ratio (to housekeeping gene β-actin) of L-type, P/Q-, N-, R-, and T-type Ca_v subunits. Experiments were performed using 3 separate extractions (n = 3).

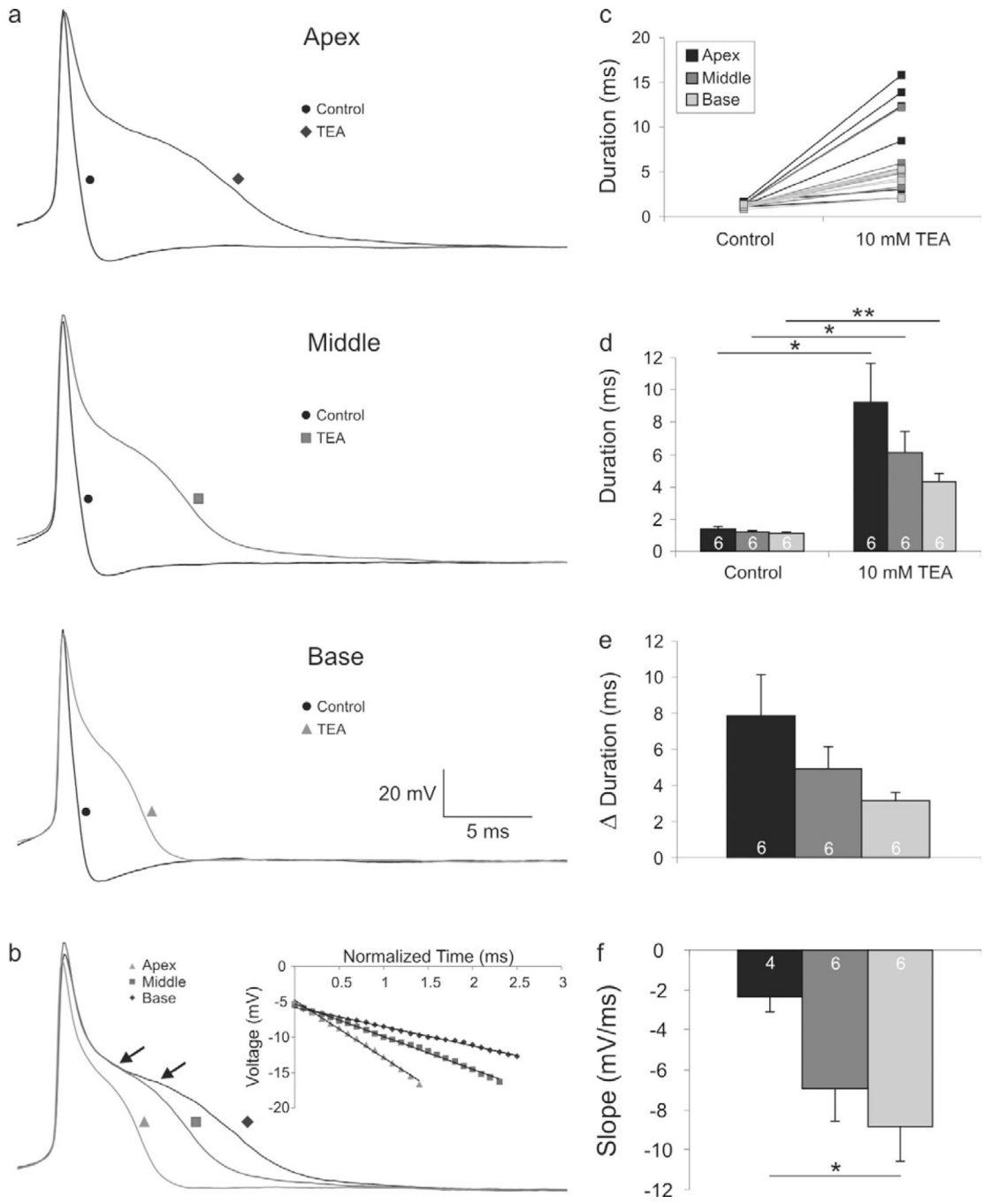

Figure 2.

Action potential repolarization is prolonged differentially in apical, middle, and basal neurons after tetraethylammonium (TEA) application. (a) Representative recordings from apical, middle, and basal neurons before (black traces labeled with circles) and after application of TEA (gray traces labeled with a diamond, square and triangle, respectively). (b) Overlaid traces of apical, middle, and base whole-cell current clamp recordings exemplifying the differences in action potential repolarization. Arrows indicate the region of measurement for slope values. Inset: calculated slope of the plateau region; $R^2 > 0.99$ for all fits. (c) Individual duration measurements before and after TEA application. (d) Averaged measurements show significant action potential duration increases in the apex, middle, and

base after TEA application. (e) Change in action potential duration before and after TEA application shows that the relative action potential duration between the apex, middle and basal neurons is retained. (f) Averaged slope measurements show a significant difference between the apical and basal neurons. (For this and subsequent figures, paired Student's *t*-test: *, $p < 0.05$; **, $p < 0.01$).

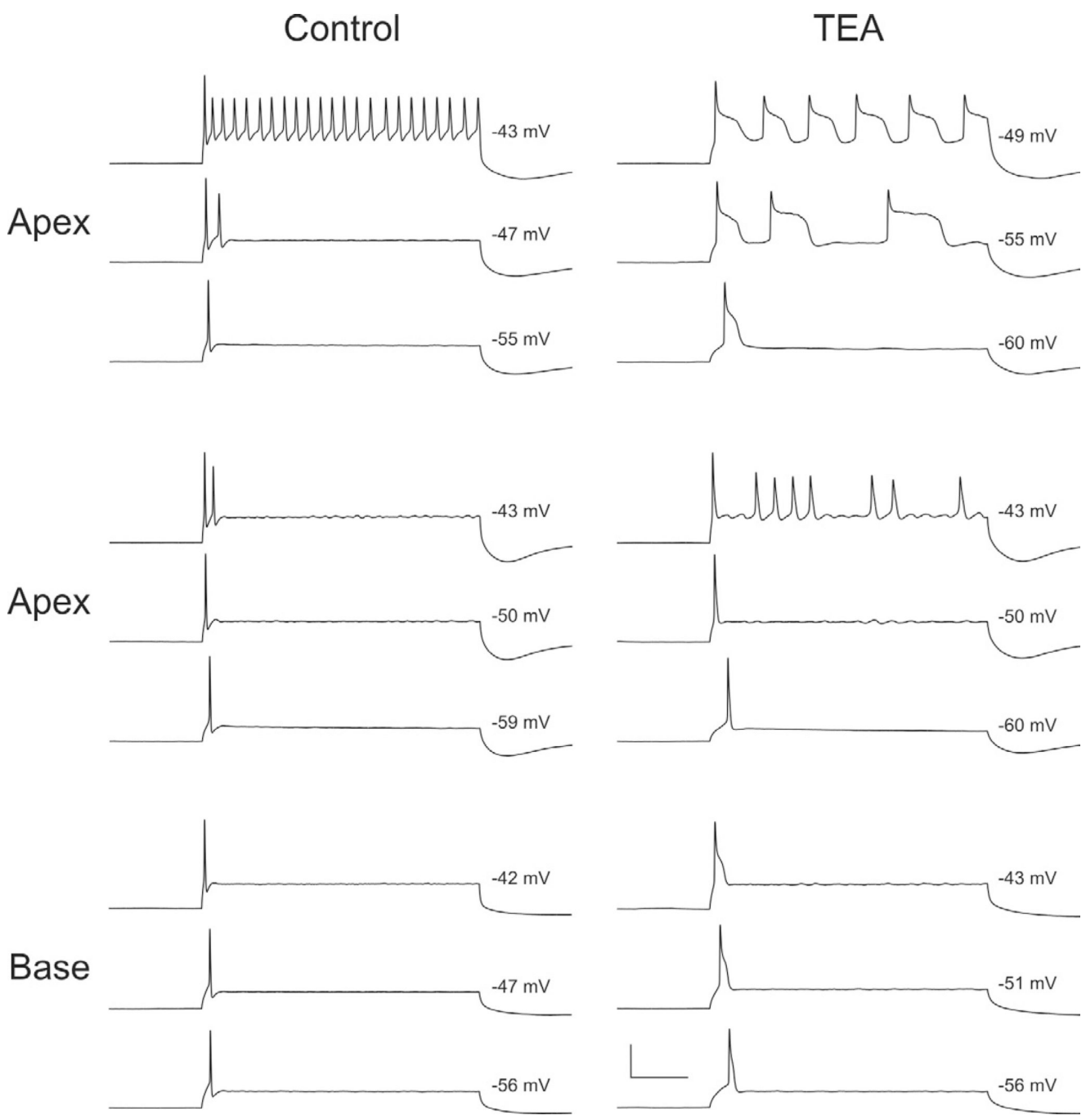

Figure 3.

Apical neurons display differential responses to TEA application. Whole-cell current clamp recordings before (Control) and after (TEA) exposure to TEA from two different apical neurons (top and middle panels) and one basal neuron. Responses are shown for threshold (lowest traces) and suprathreshold levels (middle and upper traces) for each of the three neuronal recordings. Values at the right of each trace are measured (estimated; top panel, upper traces) from the plateau potentials resulting from a prolonged constant current injection (240 ms). Of the total number of recordings made from apical, middle, and basal spiral ganglion neurons, only two apical neurons showed and absence of Ca^{2+} spikes (middle panel).

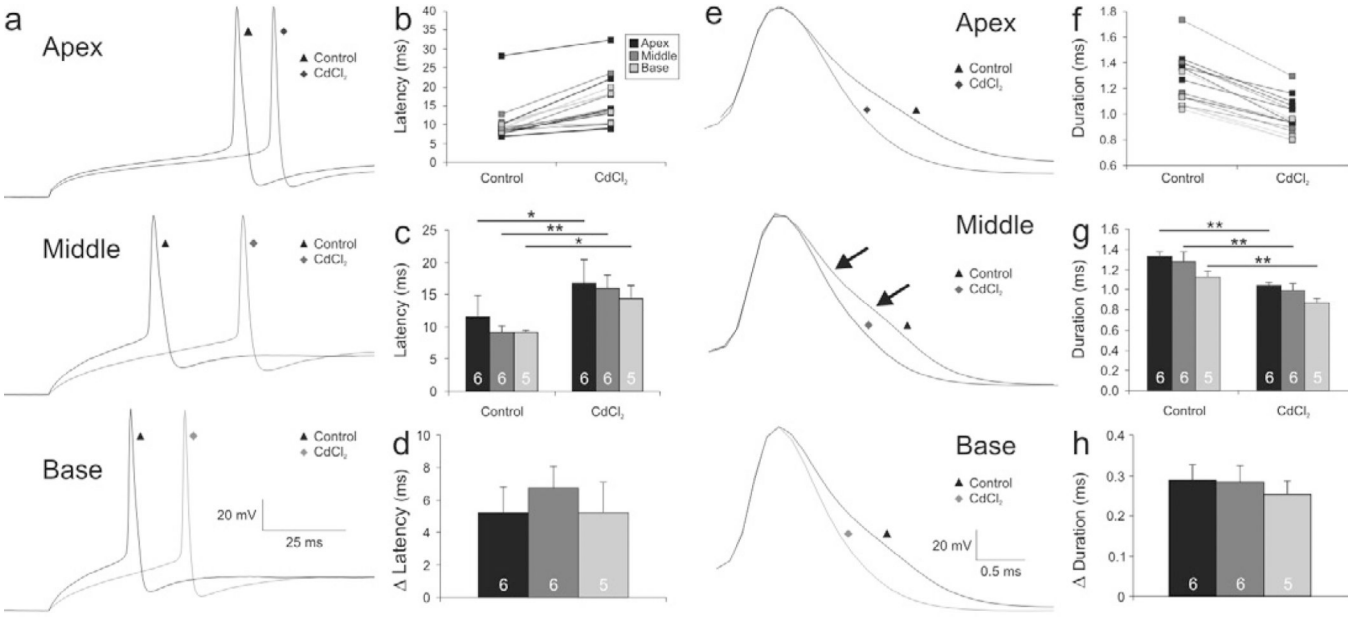

Figure 4.

Action potential latency and duration are prolonged differentially in apical, middle, and basal neurons after $CdCl_2$ application. (a) Representative whole-cell current clamp traces from apical, middle, and basal neurons exemplifying action potential latency at threshold before (black traces labeled with triangles) and after application of $CdCl_2$ (gray traces labeled with diamonds). (b) Individual latency measurements before and after $CdCl_2$ exposure. (c) Averaged measurements show significant increases in action potential latency for apex, middle, and base neuronal recordings after $CdCl_2$ application. (d) Change in latency before and after the $CdCl_2$ application. (e) Representative traces aligned at peak action potential voltage exemplifying action potential duration differences of apical, middle, and basal recordings before (black traces labeled with triangles) and after application of $CdCl_2$ (gray traces labeled with diamonds). (f) Individual duration measurement before and after $CdCl_2$ application. (g) Averaged measurements show significant differences in action potential duration for recordings made from apex, middle, and basal neurons exposed to $CdCl_2$. (h) Change in duration before and after $CdCl_2$ application.

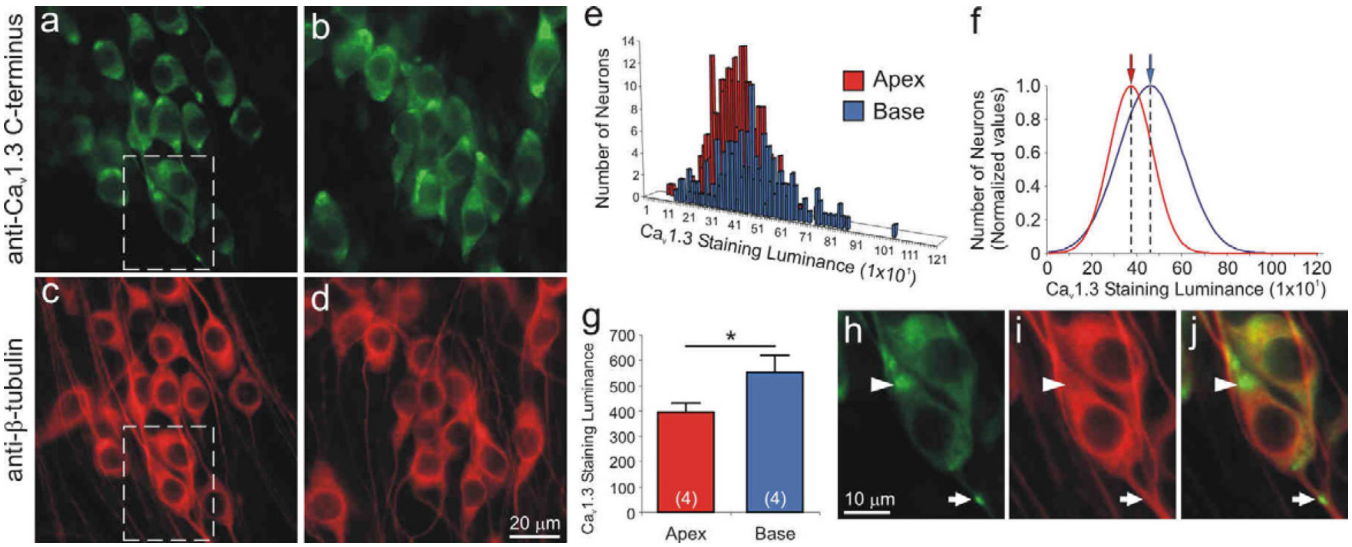

Figure 5.

The $Ca_v1.3$ α-subunit was localized predominantly in basal spiral ganglion neurons. Neurons labeled with anti-$Ca_v1.3$ C-terminus antibody (green) showed differential immunofluorescence in (a) apex and (b) base neurons. (c, d, i) Anti-β-tubulin antibody (red) was used as a neuron-specific marker, which showed relatively uniform labeling. Dotted area in panels a and c was magnified in panel h and i, respectively. (e) Representative histograms of apex and base $Ca_v1.3$ staining luminance in a single experiment were (f) normalized and fitted with Gaussians; means for apical and basal neurons indicated by arrows (red and blue, respectively). (g) Averaged anti-$Ca_v1.3$ antibody luminance ($n = 4$) was significantly higher in the base than in the apex (*, $p < 0.05$). (h) Anti-$Ca_v1.3$ antibody was clustered at the poles of cell somata (arrowhead) and occasionally along neurites (arrow). (j) Overlay of β-tubulin and $Ca_v1.3$ staining luminance. Calibration bars in panels d and h apply to panels a–d and h–j, respectively.

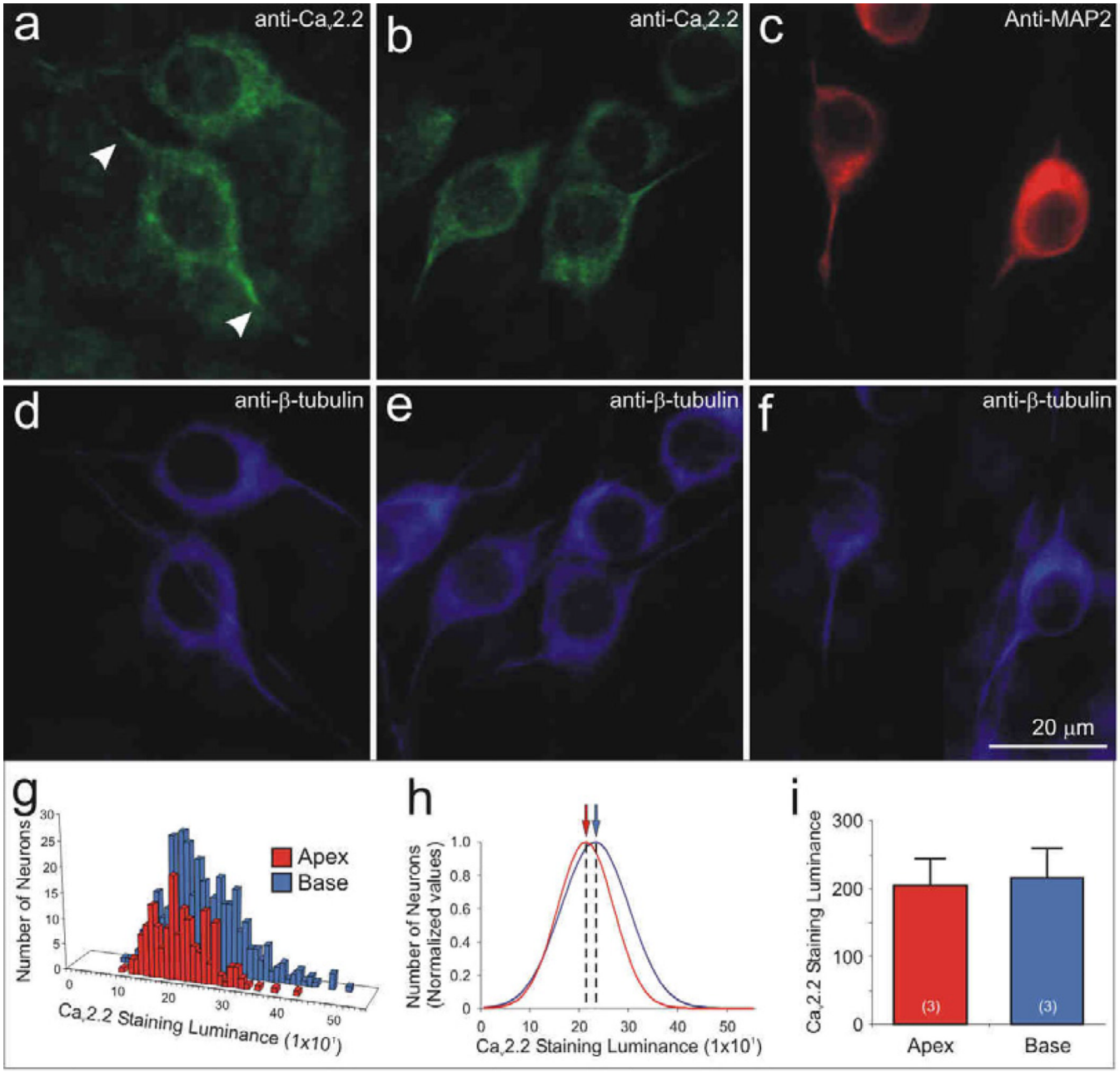

Figure 6.

The $Ca_V2.2$ α-subunit was uniformly distributed within apical and basal neurons, yet showed an unique intracellular pattern, similar to that observed for MAP2 labeling. Anti-$Ca_V2.2$ α-subunit antibody (green) labeling showed similar staining intensity in (a) apex and (b) neurons. The intracellular distribution, however, was distinctive because labeling of the somata extended for restricted distances into the initial regions of the processes (a, arrowheads), despite observations that the processes labeled with anti-β-tubulin antibody extended well beyond that point (d), often for hundreds of microns (not shown). (c) Neurons labeled with anti-MAP2 (red) showed a similar intracellular labeling pattern observed with anti-$Ca_V2.2$, such that enriched labeling was confined to the soma and initial processes. (d–

f) Anti-β-tubulin antibody (blue) was used as a neuron-specific marker showing that the length of the processes extended beyond anti-$Ca_V2.2$ and anti-MAP2 immunolabeling. Neuronal measurements of anti-$Ca_V2.2$ luminance were illustrated by (g) representative histograms and (h) normalized Gaussian distributions for a single experiment. (i) Averaged $Ca_v2.2$ staining luminance ($n = 3$) showed that anti-$Ca_v2.2$ antibody luminance was similar between the two regions. Calibration bar in panel f applies to a–f.

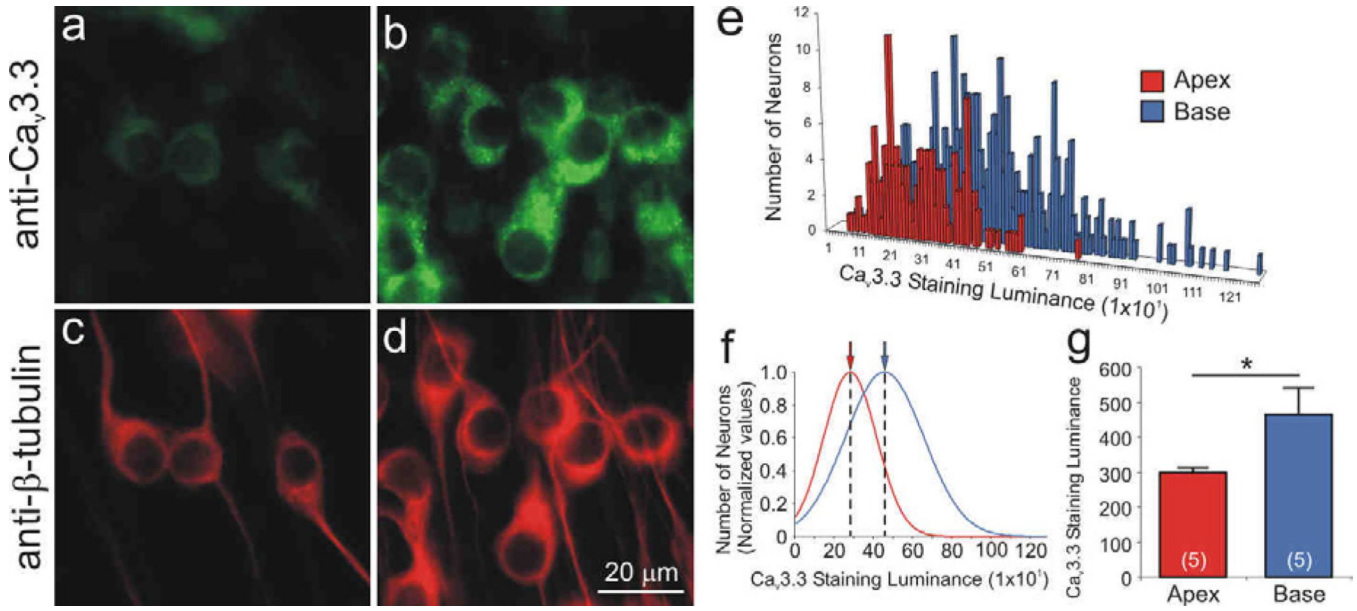

Figure 7.

The $Ca_v3.3$ α-subunit was differentially localized in spiral ganglion neurons with greater staining intensity in the basal neurons relative to the apical neurons. Neurons labeled with anti-$Ca_v3.3$ antibody (green) showed differential intensity in (a) apex and (b) base. Immunolabeling was confined mainly to the neuronal somata. (c–d) Anti-β-tubulin antibody (red) was used as a neuron-specific marker. Anti-$Ca_v3.3$ antibody luminance illustrated by (e) representative histograms and (f) normalized Gaussian distributions for a single experiment. (g) Averaged anti-$Ca_v3.3$ antibody luminance was significantly higher in the base than in the apex (n = 5). Calibration bar in panel d apply to panels a–d.

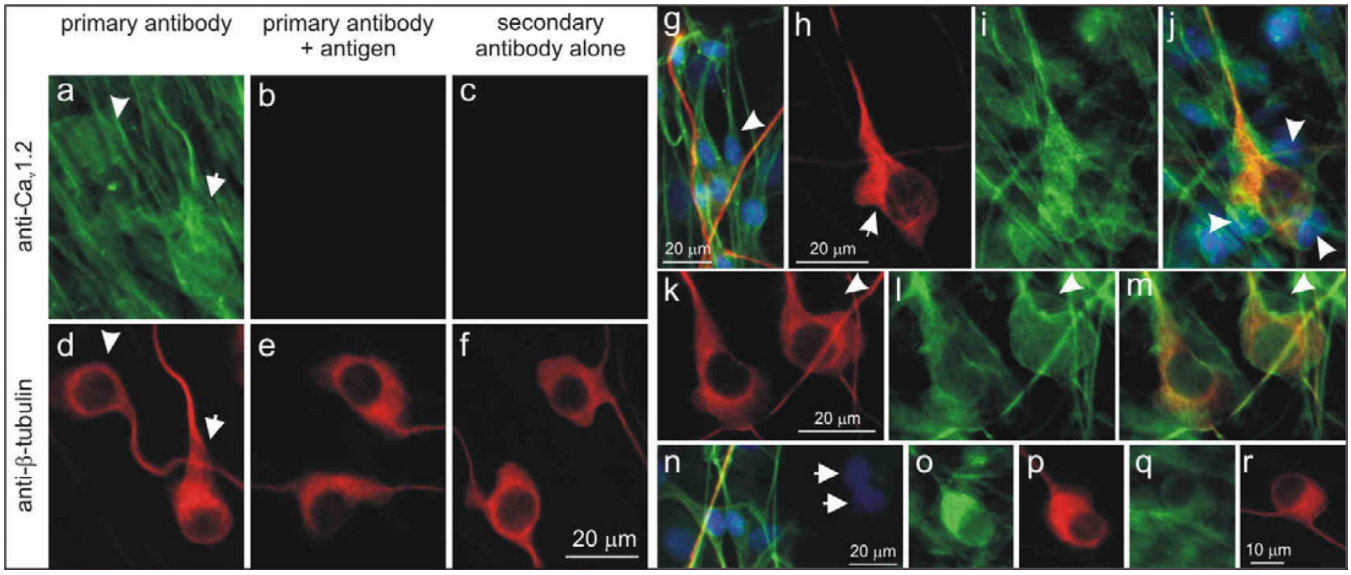

Figure 8.

The $Ca_V1.2$ α-subunit was present in both neurons and satellite cells in the spiral ganglion and was associated with myelination. (a) Control experiments confirmed the specificity of anti-Cav1.2 antibody. Neurons (arrow, arrowhead) and satellite cells were labeled with anti-$Ca_V1.2$ antibody (green). (b) Antibody pre-incubated with control antigen peptide showed little or no anti-$Ca_V1.2$ antibody labeling. (c) Little or no immunofluorescence was observed in secondary antibody alone controls. (d–f) Anti-β-tubulin antibody (red) was used as a neuronal marker. (g) Anti-$Ca_V1.2$ antibody (green) labeled the soma and processes of bipolar spindle-shaped satellite cells (arrowhead) with a morphology that resembled Schwann cells. Hoechst dye (blue) was utilized to highlight cell nuclei, neurons and their processes were labeled with anti-β-tubulin (red). (h–j) Schwann cells surrounded the cell body of a neuron (arrowhead) and were aligned along neuronal processes (h) anti-β-tubulin (red), (i) anti-$Ca_V1.2$ (green), (j) overlay with Hoechst dye (blue). (k–m) A sub-set of neurons were encapsulated by $Ca_V1.2$ immunofluorescent structures resembling loose myelin sheaths that surround spiral ganglia somata; arrowheads indicate a putative Schwann cell soma. (k) anti-β-tubulin (red), (l) anti-$Ca_V1.2$ (green), (m) overlay. (n) Two non-immunoreactive satellite cells (arrows); overlay of anti-$Ca_V1.2$ (green), anti-β-tubulin (red), Hoechst dye (blue). Neurons stained with different intensities: (o) brightly-stained neuron, (q) lightly-stained neuron. (p, r) Anti-β-tubulin antibody. Calibration bar in panel a applies to a–f; h applies to h–j; k applies to k–m; r applies to o–r.

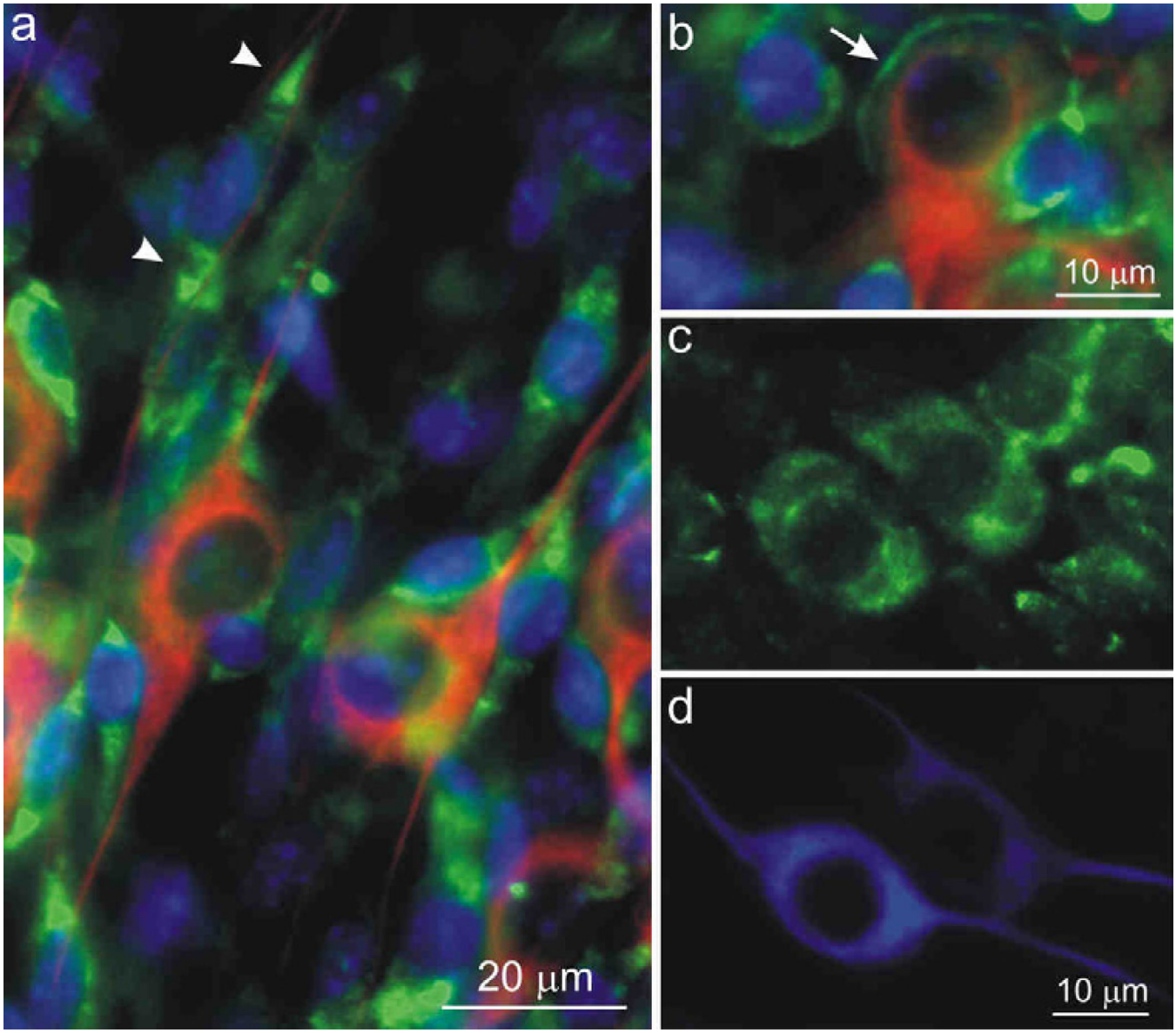

Figure 9.

The $Ca_v2.1$ α-subunit was present in both neurons and satellite cells in the spiral ganglion. (a) Anti-$Ca_v2.1$ antibody (green) labeled the bipolar putative Schwann cells (arrowheads) on either side of their nuclei (Hoechst dye, blue); spiral ganglion neurons labeled with anti-β-tubulin antibody (red) were in close proximity. (b) The process of a Schwann cell (arrow, anti-$Ca_V1.2$, green) wrapped around neuron's cell body (anti-β-tubulin, red); Hoechst dye (blue). (c) Anti-$Ca_v2.1$ antibody (green) labeled the cell body of neuron with distinct intracellular distribution patterns. (d) Anti-β-tubulin antibody (blue) was used as a neuron-specific marker. Calibration bar in panel d applies to c–d.

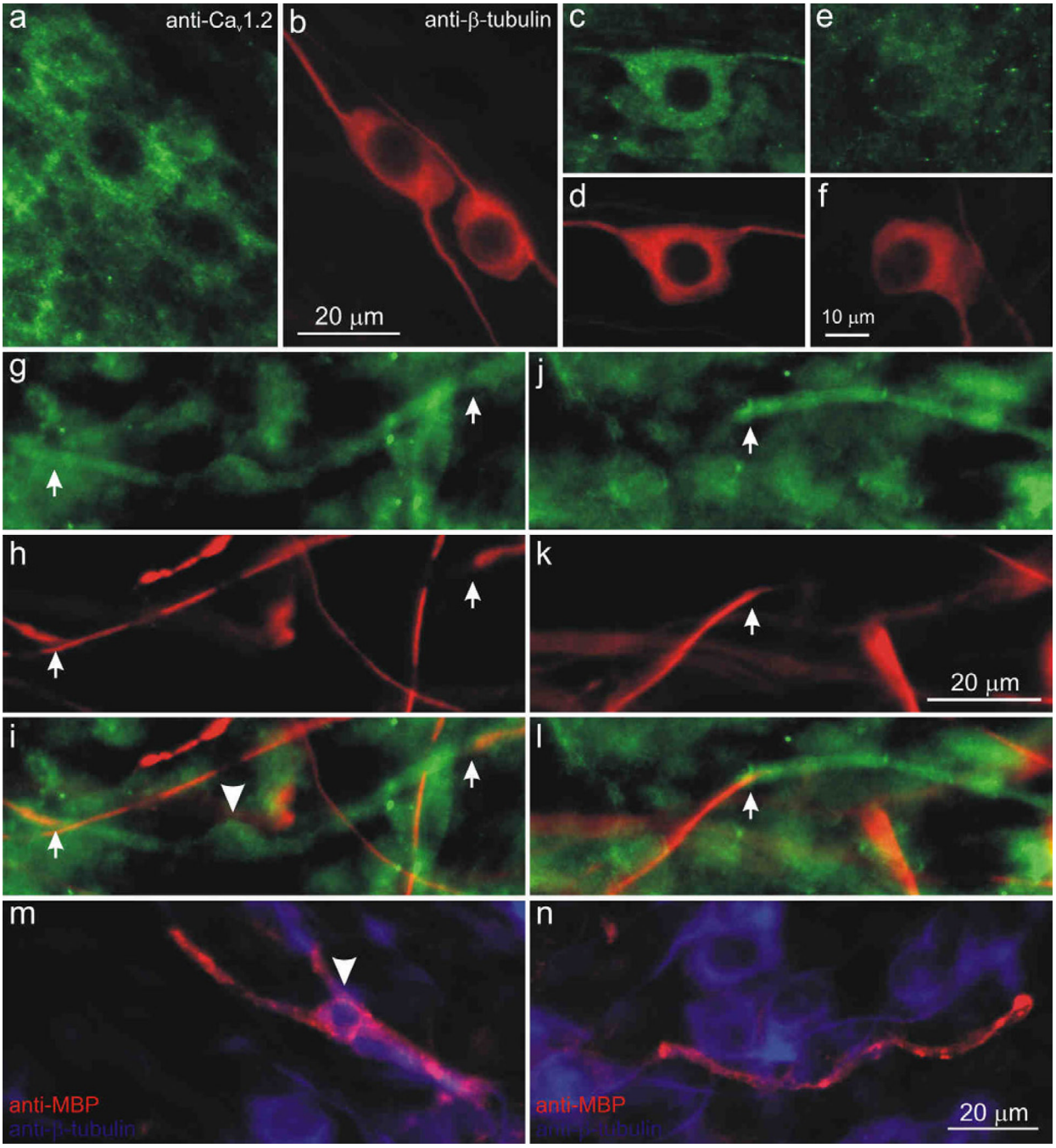

Figure 10.

The $Ca_V2.3$ α-subunit was present in both neurons and satellite cells in the spiral ganglion and was associated with compact myelin. (a) Anti-$Ca_V2.3$ antibody (green) stained for neurons and satellite cells. (b, d, f, h, k) Anti-β-tubulin antibody (red) was used as a neuron-specific marker. Instances in which surrounding satellite cells did not preclude visualization, anti-$Ca_V2.3$ antibody (green) was enriched in a small number of neurons (c), while most neurons (e) were lightly labeled. (g, j) anti-$Ca_V2.3$ immunofluorescence (green) was detected in a compact myelin-like structure (between arrows) that surrounded (h, k) anti-β-tubulin-labeled neurites. (i,l) Overlay images from g, h and j, k, respectively (arrowhead in i indicates the soma profile of a putative Schwann cell. (m, n) Overlaid images of anti-myelin

basic protein (SMI-99, red) surrounded neuronal processes (anti-β-tubulin, blue), which appeared similar to structures labeled by anti-$Ca_V2.3$ in panels g–l. Arrowhead (m) indicates the soma profile of a myelinating Schwann cell. Calibration bar in b applies to a–b; f applies to c–f; k applies to g–l; n applies to m–n.

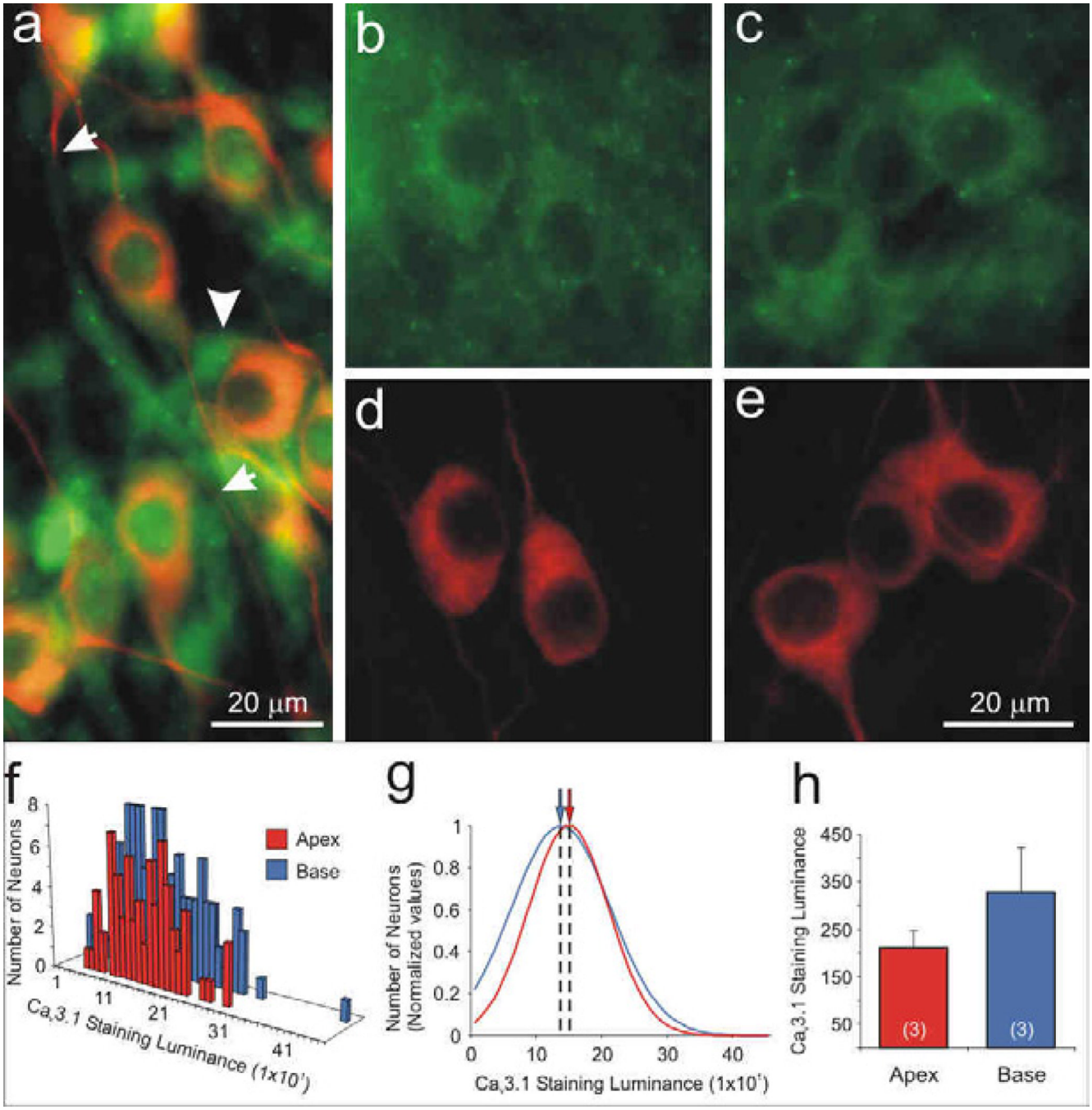

Figure 11.

The $Ca_V3.1$ α-subunit was localized to satellite cells, compact-myelin-like structures, and uniformly labeled apical and basal spiral ganglion neurons. (a) anti-Cav3.1 antibody labeled satellite cells diffusely (arrowhead) as well as regions detected in a compact myelin-like structure (between arrows) that surrounded an anti-β-tubulin-labeled neurite (red). In areas with lower levels of surrounding satellite cells, we were able to detect neuronal labeling with anti-$Ca_V3.1$ antibody (green), which showed similar intensity levels in (b) apex and (c) base neurons. (d–e) Anti-β-tubulin antibody (red). Anti-$Ca_V3.1$ antibody staining luminance is illustrated by (f) representative histograms and (j) normalized Gaussians for a single

experiment. (h) Averaged anti-$Ca_v3.1$ immunofluorescence did not differ systematically between apical and basal neurons ($n = 3$; $p > 0.20$). Calibration bar in panel e applies to b–e.

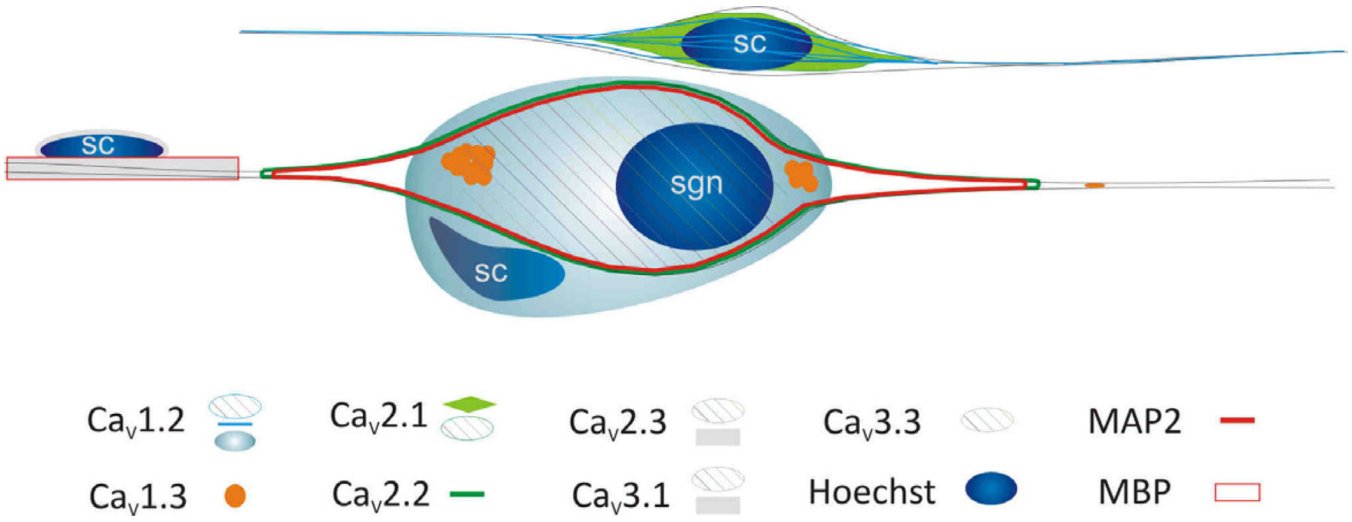

Figure 12.
Schematic summary of VGCC α-subunit localization in a neuron and Schwann cells. Abbreviations: sgn = spiral ganglion neuron; sc = Schwann cell; MAP2 = microtubule associated protein 2; MBP = myelin basic protein.

Table 1

Primer information for real-time quantitative RT-PCR.

Name	Sense primer	Antisense primer
$Ca_v1.1$	Nucleotides 1159–1180	Nucleotides 1259-1238
(accession No. NM_014193)	5'-GAA CCT TCC AAA AGC TCC GAG-3'	5'-CAA GTC GTC CAC GTC CAT GAC-3'
$Ca_v1.2$	Nucleotides 3868–3888	Nucleotides 3968-3943
(accession No. AY728090)	5'-TGC CTT CAA ACC CAA GCA CT-3'	5'-GGT GTA CCT CGG TGA TTG CTA TAT C-3'
$Ca_v1.3$	Nucleotides 3316–3337	Nucleotides 3416-3392
(accession No. NM_028981)	5'-TTT GAC AAT GTC CTT TCG GCT-3'	5'-TTC TCA CCG TTT GAA TCA ATA GCT-3'
$Ca_v1.4$	Nucleotides 4029–4052	Nucleotides 4129-4110
(accession No. NM_019582)	5'-CTT CAT CTA TGC AGT CAT TGG CA-3'	5'-CCT GCG GAA AGG TCT GGA A-3'
$Ca_v2.1$	Nucleotides 891–911	Nucleotides 991-971
(accession No. NM_007578)	5'-CAT CAT CAT CGG CTC CTT TT-3'	5'-GAA AAG CTC TCC GGT TCT CC-3'
$Ca_v2.2$	Nucleotides 3665–3685	Nucleotides 3765-3746
(accession No. NM_007579)	5'-GAA AAG CTC TCC GGT TCT CC-3'	5'-TTT AGG CAG CCG CTT GAT G-3'
$Ca_v2.3$	Nucleotides 534–554	Nucleotides 634-614
(accession No. NM_009782)	5'-AAC CCA CTT CAA CAC CCA CG-3'	5'-GCA CGA TCT GCA GGC TAG GT-3'
$Ca_v3.1$	Nucleotides 2040–2059	Nucleotides 2140-2124
(accession No. NM_009783)	5'-CGC TGA CCA TGA AAT GCC T-3'	5'-GCC GTC GCC GTC TGT G-3'
$Ca_v3.2$	Nucleotides 301–322	Nucleotides 401–420
(accession No. NM_021415)	5'-TGG TTC GAG CAC ATT AGC ATG-3'	5'-CTG CAA CGT TCT GAA CGG C-3'
$Ca_v3.3$	Nucleotides 919–939	Nucleotides 1019-999
(accession No. AY026384)	5'-GGG CAT CAG TGG CTG TAG TT-3'	5'-GTG CAC CCT GAA TTG CTT CT-3'
β-actin	Nucleotides 850–870	Nucleotides 900-880
(accession No. X03672)	5'-GCC CTG AGG CTC TTT TCC AG-3'	5'-TGC CAC AGG ATT CCA TAC CC-3'

Table 2

Antibody information for immunocytochemistry.

Antigen	Company and Identification No.	Host, Immunogen	Fixation Method	Working Dilution
$Ca_v1.2$	Alomone (Jerusalem, Isreal), ACC-003, lot AN-18	Rabbit polyclonal, seq 848–865 aa, intracellular loop between domain II–III	4% PFA	1:75
$Ca_v1.3$	NeuroMab (Davis, CA), 75-080	Mouse monoclonal, clone N38/8, fusion protein 2025–2161 aa, C-terminus	Methanol	1:100
$Ca_v2.1$	Alomone (Jerusalem, Isreal), ACC-001, lot AN-09	Rabbit polyclonal, seq 865–881 aa, intracellular loop between domain loop II–III	Methanol	1:1400
$Ca_v2.1$	Sigma-Aldrich (St. Louis, MO), C1353	Rabbit polyclonal, seq 865–881 aa, intracellular loop between domain II–III	Methanol	1:25
$Ca_v2.2$	Alomone (Jerusalem, Israel), ACC-002, lot AN-01 and −21	Rabbit polyclonal, seq 851–867 aa, intracellular loop between domain II–III	Methanol	1:400, 1:100
$Ca_v2.3$	Alomone (Jerusalem, Israel), ACC-006; lot AN-03	Rabbit polyclonal, seq 982-907 aa, intracellular loop between domain II–III	4% PFA	1:50
$Ca_v3.1$	Alomone (Jerusalem, Israel), ACC-021; lot AN-05	Rabbit polyclonal, seq 1–22 aa, N-terminus	4% PFA	1:50
$Ca_v3.3$	Alomone (Jerusalem, Israel), ACC-009, lot AN-02	Rabbit polyclonal, seq 1053–1067 aa, intracellular loop between domain II–III	Methanol	1:50
MAP-2	Millipore (Billerica, MA), AB5622, lot NG1723932	Rabbit polyclonal, microtubule-associated protein	Methanol	1:100
MBP	Sternberger Monoclonals Inc. (Lutherville, MD), lot 1	Mouse monoclonal, clone SMI-99	4% PFA	1:1000
β-tubulin	Covance (Princeton, NJ), MMS-435P	Mouse monoclonal, neuronal class III β-tubulin	Methanol / 4% PFA	1:200
β-tubulin	Covance (Princeton, NJ), PRB-435P	Rabbit polyclonal, neuronal class III β-tubulin	Methanol / 4% PFA	1:200